

BEACON: JWST NIRCam Pure-parallel Imaging Survey. II. Physical Properties of $z = 7 - 14$ Galaxies

YECI ZHANG ,¹ TAKAHIRO MORISHITA ,¹ KIMI C. KREILGAARD ,^{2,3} CHARLOTTE A. MASON ,^{2,3} ABDURRO'UF ,⁴ HAKIM ATEK ,⁵ MARUŠA BRADAČ ,^{6,7} LARRY D. BRADLEY ,⁸ ANDREW J. BUNKER ,⁹ VIOLA GELLI ,^{2,3} NOVAN SAPUTRA HARYANA ,¹⁰ MATTHEW J. HAYES ,¹¹ GEORGE HELOU ,¹ NICHA LEETHOCHAWALIT ,¹² ZHAORAN LIU ,^{10,13} MARC RAFELSKI ,^{14,15} GUIDO ROBERTS-BORSANI ,¹⁶ MICHAEL J. RUTKOWSKI ,¹⁷ CLAUDIA SCARLATA ,¹⁸ MASSIMO STIAVELLI ,¹⁹ RYO A. SUTANTO ,¹⁰ HARRY I. TEPLITZ ,²⁰ T. TREU ,²¹ M. TRENTI ,²² BENEDETTA VULCANI ,²³ AND XIN WANG ,^{24,25,26}

¹IPAC, California Institute of Technology, MC 314-6, 1200 E. California Boulevard, Pasadena, CA 91125, USA

²Cosmic Dawn Center (DAWN), Denmark

³Niels Bohr Institute, University of Copenhagen, Jagtvej 128, DK-2200 Copenhagen N, Denmark

⁴Department of Astronomy, Indiana University, 727 East Third Street, Bloomington, IN 47405, USA

⁵Institut d'Astrophysique de Paris, CNRS, Sorbonne Université, 98bis Boulevard Arago, 75014, Paris, France

⁶University of Ljubljana, Department of Mathematics and Physics, Jadranska ulica 19, SI-1000 Ljubljana, Slovenia

⁷Department of Physics and Astronomy, University of California Davis, 1 Shields Avenue, Davis, CA 95616, USA

⁸Space Telescope Science Institute (STScI), 3700 San Martin Drive, Baltimore, MD 21218, USA

⁹Department of Physics, University of Oxford, Denys Wilkinson Building, Keble Road, Oxford OX1 3RH, UK

¹⁰Astronomical Institute, Tohoku University, 6-3, Aramaki, Aoba, Sendai, Miyagi 980-8578, Japan

¹¹Stockholm University, Department of Astronomy and Oskar Klein Centre for Cosmoparticle Physics, AlbaNova University Centre, SE-10691, Stockholm, Sweden

¹²National Astronomical Research Institute of Thailand (NARIT), Mae Rim, Chiang Mai, 50180, Thailand

¹³MIT Kavli Institute for Astrophysics and Space Research, 70 Vassar Street, Cambridge, MA 02139, USA

¹⁴Space Telescope Science Institute, 3700 San Martin Drive, Baltimore, MD, 21218 USA

¹⁵Department of Physics and Astronomy, Johns Hopkins University, Baltimore, MD 21218, USA

¹⁶Department of Physics & Astronomy, University College London, London, WC1E 6BT, UK

¹⁷Minnesota State University, Mankato, Department of Physics and Astronomy, 141 Trafton Science Center N, Mankato, MN 56001, USA

¹⁸University of Minnesota, Twin Cities, 116 Church St SE, Minneapolis, MN 55455, USA

¹⁹Space Telescope Science Institute, 3700 San Martin Drive, Baltimore, MD 21218, USA

²⁰IPAC, Mail Code 314-6, California Institute of Technology, 1200 E. California Blvd., Pasadena CA, 91125, USA

²¹Department of Physics and Astronomy, University of California, Los Angeles, 430 Portola Plaza, Los Angeles, CA 90095, USA

²²School of Physics, The University of Melbourne, VIC 3010, Australia

²³INAF – Osservatorio Astronomico di Padova, Vicolo Osservatorio 5, 35122 Padova, Italy

²⁴School of Astronomy and Space Science, University of Chinese Academy of Sciences (UCAS), Beijing 100049, China

²⁵National Astronomical Observatories, Chinese Academy of Sciences, Beijing 100101, China

²⁶Institute for Frontiers in Astronomy and Astrophysics, Beijing Normal University, Beijing 102206, China

Submitted to ApJ

ABSTRACT

We present photometric properties of 161 galaxy candidates at $z = 7 - 14$ selected from the second data release (DR2) of BEACON, a JWST Cycle 2 pure-parallel NIRCam imaging program. Carefully selected from 36 independent pointings (corresponding to ~ 350 arcmin 2 sky coverage), and hence with reduced cosmic variance, our galaxy candidates provide an unbiased sample for investigating galaxy properties over a wide range of environments. We measure the physical properties, including UV continuum slope (β_{UV}), stellar mass (M_*), star formation rate (SFR), and sizes. Our highest redshift galaxy candidate at $z = 13.71 \pm 0.15$ has a remarkably bright UV luminosity of $M_{\text{UV}} = -21.19 \pm 0.08$,

making it the brightest galaxy at $z > 12$ if spectroscopically confirmed. With an extremely blue UV slope, compact morphology, and high star formation rate surface density (Σ_{SFR}), this candidate may have extremely low metallicity, high ionizing photon escape fraction, or contributions from an AGN. Among our multiple independent sightlines, we identify three fields of galaxy number overdensity with $> 3\sigma$ significance. The properties of galaxies in various environments do not exhibit significant differences, implying either that accelerated galaxy evolution in overdense regions is not yet widespread at $z > 7$, or that the current constraints are limited by sample size. Our simulations indicate that increasing the sample by an order of magnitude would allow such environmental trends to be robustly confirmed or ruled out, underscoring the importance of future pure-parallel observations.

1. INTRODUCTION

JWST has opened up a new era for high-redshift galaxy searches, extending the frontier of galaxy detection to the first 300 million years after the Big Bang ($z \sim 14$) during the earliest stages of cosmic reionization. Photometric selections with NIRCam imaging have found a large population of luminous, potentially massive galaxy candidates at very high redshifts (e.g., M. Castellano et al. 2022; R. P. Naidu et al. 2022a; S. L. Finkelstein et al. 2023; Y. Harikane et al. 2023; B. E. Robertson et al. 2023; B. Robertson et al. 2024; N. J. Adams et al. 2024; M. Franco et al. 2025) that was unanticipated by pre-JWST theoretical models and observations. A large fraction of these galaxy candidates were later confirmed by extensive spectroscopic follow-up observations (e.g., E. Curtis-Lake et al. 2023; Y. Harikane et al. 2024; S. Carniani et al. 2024; R. P. Naidu et al. 2025; G. Roberts-Borsani et al. 2025a), verifying the NIRCam photometric selection and confirming the excess of bright galaxies at $z > 10$. Possible explanations of such an excess of bright galaxies at high redshifts include: *i*) higher average luminosity of galaxies due to elevated star formation efficiency (e.g., K. Inayoshi et al. 2022; A. Dekel et al. 2023) or a top-heavy initial mass function (IMF; e.g., E. R. Cueto et al. 2024; A. Hutter et al. 2025), *ii*) more bursty/stochastic star formation than at lower redshifts, that causes more low-mass dark matter (DM) halos to host bright galaxies temporarily at certain times (e.g., C. A. Mason et al. 2023; X. Shen et al. 2023; V. Gelli et al. 2024), or *iii*) extremely low dust attenuation in the UV (e.g., C. A. Mason et al. 2023; A. Ferrara et al. 2023; F. Fiore et al. 2023; F. Ziparo et al. 2023; A. Ferrara 2024; A. Ferrara et al. 2025a,b). However, it remains a challenge to choose between these scenarios with current observations.

Another main observational challenge of characterizing bright galaxies is that they tend to be highly clustered, making even large surveys strongly affected by cosmic variance. With most previous $z > 7$ galaxy selections based on JWST data focusing on a limited number of legacy fields, it is unclear how representative they are of the entire universe. Several galaxy overden-

sities have been identified in these legacy fields (e.g. M. Castellano et al. 2023; J. M. Helton et al. 2024a,b; Z. Chen et al. 2025; Q. Li et al. 2025; L. Napolitano et al. 2025; C. Witten et al. 2025) at high redshifts with elevated star formation rate (SFR), suggesting that our current understanding of galaxy formation in the first several hundred million years may be biased towards a small number of unique sites of unusually prompt strong star formation. To overcome such potential biases from cosmic variance, it is necessary to investigate in an unbiased way the general properties of galaxies in the early universe with multiple independent sight-lines that supplement the legacy fields.

Pure-parallel observations offer an ideal opportunity to conduct such studies. Since the early 2010s, several HST pure-parallel programs have successfully identified luminous ($M_{\text{UV}} = -21 \sim -23$) galaxy candidates at $z \sim 8 - 11$ (e.g., M. Trenti et al. 2011; L. D. Bradley et al. 2012; T. Morishita et al. 2020; S. Rojas-Ruiz et al. 2020; T. Morishita 2021; G. Roberts-Borsani et al. 2022, 2025b; S. Rojas-Ruiz et al. 2025). Pure-parallel programs with JWST slitless spectroscopy also allow direct redshift confirmation of galaxies up to $z = 9$ with strong emission lines (e.g., M. A. Malkan et al. 2025; F. Sun et al. 2025). JWST NIRCam, covering the rest-UV and optical wavelengths, now allows us to extend such attempts out to $z > 10$, and study galaxy properties and luminosity functions over a wide range of environments at cosmic dawn (see also C. C. Williams et al. 2025, for an overview of the Cycle 1 NIRCam pure-parallel program, PANORAMIC).

Here we present analysis of 161 galaxy candidates at $z > 7.3$ selected from the data release 2 (DR2) of the Bias-free Extragalactic Analysis for Cosmic Origins with NIRCam (BEACON) program²⁷ (GO-3990; PI: T. Morishita; Co-PIs: C. Mason, T. Treu, M. Trenti; T. Morishita et al. 2025a), a Cycle 2 NIRCam pure-parallel imaging program optimized for detections of $z > 7.3$

²⁷ The data products of BEACON DR2 will be available at <https://beacon-jwst.github.io/data.html>.

Lyman break galaxies over a total of 69 independent pointings (equivalent to 670 arcmin^2). In this work, we make use of 36 pointings (covering $\sim 350 \text{ arcmin}^2$) from BEACON data that are covered by ≥ 6 filters where robust selections of $z > 7.3$ Lyman break galaxy candidates can be performed. To investigate whether the physical properties of galaxies differ between the bias-free pure-parallel fields and legacy fields, we carefully analyze the galaxy properties, including photometric redshift, of these galaxy candidates, and investigate their correlations with local galaxy density. The UV luminosity functions and clustering properties of the same galaxy sample will be presented in the accompanying paper (Kreilgaard et al., in preparation).

This paper is structured as follows. We describe the BEACON DR2 in Section 2, followed by the $z \gtrsim 7$ galaxy candidate selection in Section 3. We detail the spectral energy distribution (SED) fitting procedure in Section 4, and present the derived galaxy properties in Section 5. In Section 6, we investigate the sizes of our sample through simple image analysis. Section 7 details a remarkably bright galaxy at $z = 13.7$ and discusses how galaxy properties differ in various environments. Throughout the paper, we use AB magnitudes and the cosmological parameters of $\Omega_m = 0.3$, and $\Omega_\Lambda = 0.7$, $H_0 = 70 \text{ km s}^{-1} \text{Mpc}^{-1}$.

2. DATA

Here we summarize the BEACON DR2 NIRCam imaging data and multiband photometric catalog construction. We refer the reader to T. Morishita et al. (2025a) for the details of the survey design and data reduction.

BEACON DR2 includes 69 independent pointings observed in parallel with primary observations, taken from 2023 October to 2024 December. Each pointing was observed with two to sixteen NIRCam medium/broad band filters, with the exposure times for each filter ranging from 408 s to 18940 s. To ensure a robust selection of $z \gtrsim 7$ galaxy candidates, we limit our analyses to 36/69 pointings that are covered by six or more broad/medium band filters, resulting in a total sky coverage of 350 arcmin^2 .

The imaging data in these 36 pointings are reduced following the procedures outlined in T. Morishita et al. (2025a). Briefly, we retrieved the raw-level images from the Mikulski Archive for Space Telescopes (MAST) archive and reduced them with the official JWST pipeline, with additional steps including $1/f$ -noise subtraction using `bbpn`²⁸, “snowball” masking us-

ing `Grizli` (G. Brammer et al. 2022), and additional cosmic-ray masking using `lacosmic` (P. G. van Dokkum 2001; L. Bradley 2023). The final drizzled images, with a pixel scale set to $0.^{\prime\prime}0315 / \text{pixel}$, are aligned to the IR-detection image (i.e., inverse-variance-weighted sum of F277W, F356W, and F444W).

We perform source detection and photometry using `Source Extractor` (E. Bertin & S. Arnouts 1996). To ensure accurate color measurement, we first match the point spread functions (PSFs) of each filter image to that of the F444W image in each pointing. We generate PSFs in each filter with `stpsf`²⁹, which are then fed to `pypher` (A. Boucaud et al. 2016) to generate the convolution kernels for each filter. We run `Source Extractor` in dual image mode, performing source detection in the detection images and photometry in each PSF-matched filter image. The key configuration parameters of `Source Extractor` are set as follows: `DETECT_MINAREA` 0.0081 arcsec^2 , `DETECT_THRESH`=1.0, `DEBLEND_NTHRESH`=64, `DEBLEND_MINCONT`=0.0001, `BACK_SIZE`=128, and `BACK_FILTSIZE`=5. We measure the source fluxes within fixed apertures of $0.^{\prime\prime}16$ radii, and then scale them to the total fluxes with a single factor for each source, defined as $f_{\text{auto}, \text{F444W}} / f_{\text{aper}, \text{F444W}}$, where f_{auto} is the flux measured within elliptical Kron apertures with a 2.5 scaling factor (E. Bertin & S. Arnouts 1996). Finally, we correct for the Galactic dust reddening using the attenuation value retrieved for the coordinates of each field from NED (D. J. Schlegel et al. 1998; E. F. Schlafly & D. P. Finkbeiner 2011), assuming the Milky Way reddening law (J. A. Cardelli et al. 1989).

3. SAMPLE SELECTION

From the multiband source catalog constructed in Section 2, we select $z \gtrsim 7$ galaxies via the Lyman break dropout method and constrain their redshift probability distribution, $p(z)$, with `EAZY` (G. B. Brammer et al. 2008). We detail the selection procedure below.

We first apply the following color selection criteria in three redshift bins:

F090W-dropouts ($7.3 \lesssim z \lesssim 9.7$)

$$S/N_{150} > 4$$

$$S/N_{090} < 2$$

$$z_{\text{set}} = 6$$

F115W-dropouts ($9.7 \lesssim z \lesssim 13$)

$$S/N_{200} > 4$$

²⁸ <https://github.com/mtakahiro/bbpn>

²⁹ <https://github.com/spacetelescope/stpsf>

$$\begin{aligned}
& S/N_{115,090} < 2 \\
& z_{\text{set}} = 8 \\
& \mathbf{F150W-dropouts} \ (13 \lesssim z \lesssim 18) \\
& S/N_{277} > 4 \\
& S/N_{150,115,090} < 2 \\
& z_{\text{set}} = 10,
\end{aligned}$$

which require 2σ non-detections for filters that are bluer than the rest-frame 1216 Å of the sources at the corresponding redshift ranges. To further ensure non-detections, we repeat the non-detection step with a smaller aperture, $r = 0.^{\prime\prime}08$ (~ 2.5 pixel). The z_{set} parameter is the redshift limit used for the z_{phot} cut (see below). For typical noise levels, these selections correspond to Lyman breaks of 0.7–4.2 magnitudes.

Next, we derive $p(z)$ of the color-selected sources with **EAZY**. We adopt the template sets in [K. N. Hainline et al. \(2024a\)](#), with the addition of dusty emission line galaxy template from [R. P. Naidu et al. \(2022b\)](#). The [K. N. Hainline et al. \(2024a\)](#) templates supplement the default **EAZY** “v1.3” library with young, high specific star formation rate (sSFR) galaxy templates generated with **fsps** ([C. Conroy et al. 2009](#)), enabling a more comprehensive redshift estimate for our target young galaxies. We set the redshift range of fitting to $0 < z < 20$ with a step size of $0.01(1+z)$. In each redshift bin considered, **EAZY** combines all of the available templates together and applies the average [P. Madau \(1995\)](#) IGM absorption. The χ^2 of the best fit in that redshift bin is recorded as $\chi^2(z)$ which is output from the program. We did not adopt any apparent magnitude priors, as the galaxy apparent magnitude - redshift relation at $z > 7$ is currently not well constrained. To prevent bright fluxes from dominating the fits, we set an error floor on the photometry of 5%. We also use the **EAZY** template error file “**TEMPLATE_ERROR.eazy_v1.0**” to account for uncertainties in the templates as a function of wavelength.

We run **EAZY** with the above settings and obtain the redshift probability distribution, $p(z)$, of each source from $\chi^2(z)$, assuming a uniform redshift prior: $p(z) = \exp[-\chi^2(z)/2]$, which is normalized such that $\int p(z)dz = 1.0$. We then apply the z_{phot} cut, requiring $p(z > z_{\text{set}}) > 0.8$, i.e., the total probability that each source is at $z > z_{\text{set}}$ must be greater than 80%, where z_{set} is defined above for each redshift bin. The combined color selection and $p(z)$ cut ensure the selected sources have redshifts consistent with the redshift range of the dropout selections. With these procedures, we obtain 266 sources.

From here, we conduct visual inspections on the 266 sources, rejecting data artifacts consisting of extended

diffraction spikes from stars, bad pixels, and hot pixels caused by cosmic rays in any of the available filters that may affect the photometry. We are left with 166 candidates after visual inspection, including 151, 14, and one sources with F090W-dropouts, F115W-dropouts, and F150W-dropouts, respectively. These sources represent our final sample of $z \gtrsim 7$ galaxy candidates.

One main source of contamination for high- z galaxy selection is foreground low-mass stars (T-, L-, M-type stars, i.e., brown dwarfs), which have similar spectral features to high- z galaxies such as the color break at observed $\sim 1 \mu\text{m}$ ([T. Morishita 2021](#); [K. N. Hainline et al. 2024b](#); [J. E. Greene et al. 2024](#)). To assess such contamination, we use **EAZY** to fit the dwarf templates from **SPEX** library ([J. T. Rayner et al. 2003](#)) to our 166 galaxy candidates at $z > 7$, fixing the redshifts to zero. We find that for all 166 objects, the best-fit $z > 7$ galaxy SEDs have lower χ^2 than the best-fit dwarf SEDs, suggesting that our high- z galaxy sample is unlikely to contain many foreground brown dwarfs.

Next, we examine the accuracy of the $p(z)$ derived by **EAZY**. We cross-match our 166 candidates with public JWST spectroscopy, using the spectroscopic catalog from Dawn JWST Archive (DJA) v4.4. We find 14/166 objects in our final catalog of $z \gtrsim 7$ galaxy candidates have reliable z_{spec} measurements in the DJA catalog. All of these 14 galaxies have **zgrade**=3 in the DJA catalog, with z_{spec} measured by strong emission lines in the PRISM or medium resolution spectra. In the top panel of Figure 1, we compare the **EAZY** photometric redshift (z_{EAZY}) with z_{spec} of these 14 objects. All 14 objects are confirmed to be $z > 7$ galaxies, and their z_{EAZY} is consistent with z_{spec} within the errors of $|z_{\text{phot}} - z_{\text{spec}}|/(1+z_{\text{spec}}) < 0.15$, indicating that our sample selection effectively excludes low- z interlopers. We further quantify the quality of z_{EAZY} with mean absolute error (MAE) and median absolute deviation (NMAD), which are defined in the following equations:

$$\sigma_{\text{MAE}} = \frac{\sum_{i=0}^N |\Delta z_i|}{N}, \quad (1)$$

$$\sigma_{\text{NMAD}} = 1.48 \times \text{median} \left\{ \frac{|\Delta z - \text{median}(\Delta z)|}{1+z_{\text{spec}}} \right\}, \quad (2)$$

where $\Delta z = z_{\text{EAZY}} - z_{\text{spec}}$. We obtain $\sigma_{\text{MAE}} = 0.288$ and $\sigma_{\text{NMAD}} = 0.019$, indicating the good quality of **EAZY** photometric redshifts. We fix the redshift of these galaxies to z_{spec} when conducting SED fitting in the following section.

4. SED FITTING

To derive the physical properties of photometric redshift (z_{phot}), M_* , and SFR, for our $z \gtrsim 7$ galaxy candidates, we conduct SED fitting with **Prospector** ([B. D.](#)

Table 1. Summary of the 10 free parameters used for the SED fitting with **Prospector**

Parameter	Description	Prior
z_{phot}	Redshift	$p(z)$ obtained from Eazy (Section 2) or fixed to z_{spec}
$\log(Z/Z_{\odot})$	Stellar metallicity	tophat: min=-2.0, max=0.0
$\log(M_{*}/M_{\odot})$	Total stellar mass formed	tophat: min=6.0, max=11.0
SFH	flexible SFH: ratio of the SFRs in adjacent time bins of the five-bin SFH (four parameters in total);	student T: $\mu=0.0$, $\tau=0.3$, $\nu=2.0$
$\hat{\tau}_{\text{dust},2}$	diffuse dust optical depth	tophat: min=0.0, max=2.0
$\log U$	ionization parameter for nebular emission	tophat: min=-3.5, max=-1.0

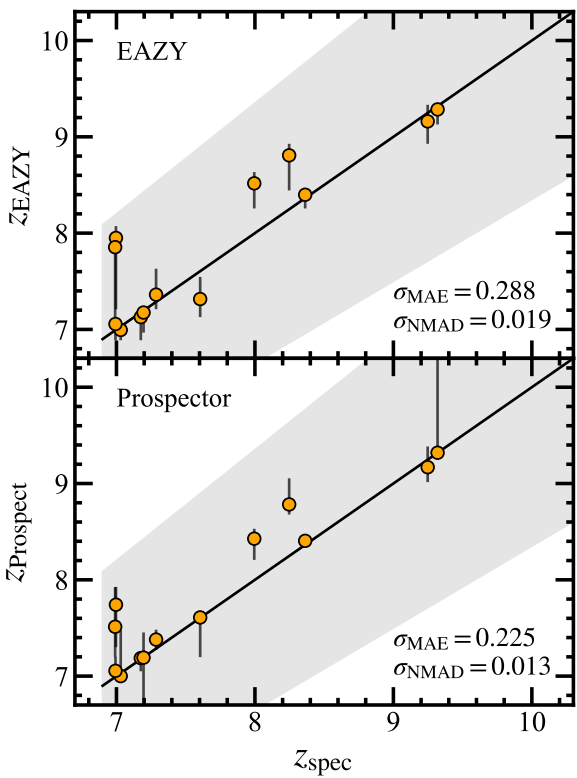


Figure 1. Top: Comparison between **EAZY** photometric redshift and spectroscopic redshift in our sample. The black solid line indicates one-to-one relation, while the grey shaded region shows the $|z_{\text{phot}} - z_{\text{spec}}| / (1 + z_{\text{spec}}) < 0.15$. Bottom: similar to the top panel, but for **Prospector** photometric redshift.

Johnson et al. 2021). The model spectra are generated from the Flexible Stellar Population Synthesis (FSPS; C. Conroy et al. 2009; C. Conroy & J. E. Gunn 2010)

package with the Modules for Experiments in Stellar Astrophysics Isochrones and Stellar Tracks (MIST; J. Choi et al. 2016) that includes the boost of the ionizing flux production of massive stars (J. Choi et al. 2017). The redshift is set to have the range of $0 < z < 20$, with the prior $p(z)$ obtained from **EAZY** fitting in Section 3 for each candidate. We assume a G. Chabrier (2003) IMF, and set the priors of M_{*} to be a tophat distribution with $6.0 \leq \log(M_{*}/M_{\odot}) \leq 12.0$. We assume a constant galaxy stellar metallicity Z with a tophat prior of $-2 \leq \log(Z/Z_{\odot}) \leq 0$. For the SF history, we adopt a non-parametric continuity SFH (J. Leja et al. 2019) with N_{SFH} time bins, where the SFR in each bin is constant. We adopt $N_{\text{SFH}} = 5$, with the first time bin fixed at 0–10 Myr of look-back time to capture the most recent variation in the SFH, while the remaining four bins are spaced equally in logarithm between the look-back time of 10 Myr and at $z = 20$. We model the dust attenuation with the SMC dust extinction law (K. D. Gordon et al. 2003), setting the attenuation A_V to have a tophat prior with the range of $0.0 \leq A_V \leq 2.0$. For the nebular attenuation, we fix the gas-phase metallicity to Z . We assume a tophat prior for the ionization parameter (U) with $-3.5 \leq \log U \leq -1.0$. The model spectra are then attenuated with the redshift-dependent P. Madau (1995) average intergalactic medium (IGM) attenuation model. The summary of free parameters and their priors is listed in Table 1.

We fit our SED model to the photometric data (Section 2), obtaining the posterior SEDs and the posterior distributions of the free parameters listed in Table 1 using the Markov Chain Monte Carlo method implemented by EMCEE. We adopt the maximum-likelihood value as the best-fit estimate and quote uncertainties based on the inner 68th percentile of the posterior distribution. Figure 2 shows examples of our best-fit SED models. Upon visual inspection on the SED fitting results, we find that most of our objects are well fitted

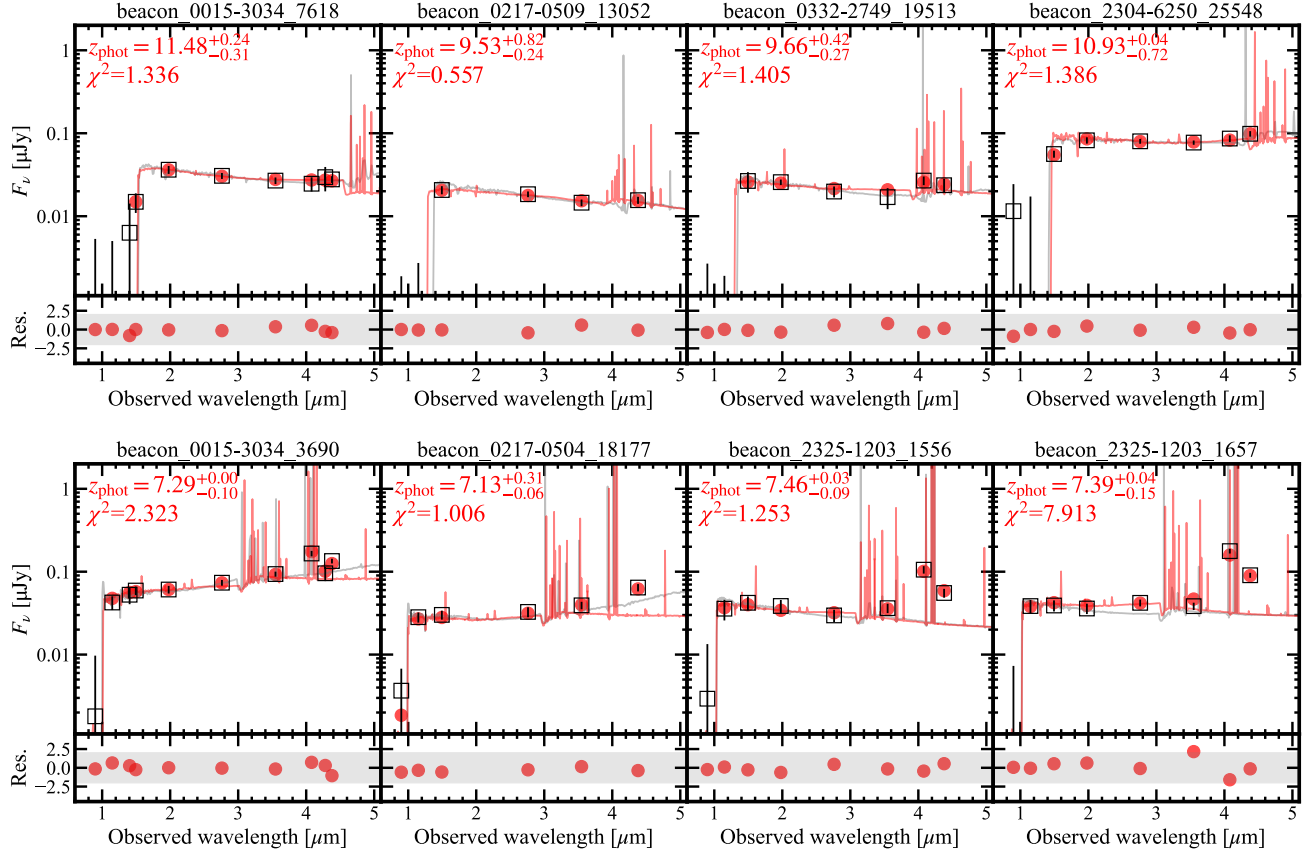


Figure 2. Examples of our SED fitting results. In the top of each panel, we show the best-fit SEDs from **EAZY** and **Prospector** with grey and red curves, respectively. The red solid circles and black open squares indicate the photometry predicted from the best-fit SEDs and the observed photometry, respectively. The normalized residuals are presented in bottom of each panel, with the horizontal shaded region showing the $\pm 2\sigma$ interval.

by our SED models, with the residuals between models and observed photometry smaller than 2σ . However, there are 5/166 objects whose rest-frame optical color is relatively red and the best-fit SED models significantly deviate from the photometric data. We examine their rest-frame UV and optical colors in Figure 3, finding that the color of these six candidates are consistent with that of compact, red sources, i.e. “little red dots” (LRD), at $z > 6$ found in multiple JWST studies (e.g., H. B. Akins et al. 2023; L. J. Furtak et al. 2023; D. D. Kocevski et al. 2023; G. Barro et al. 2024; J. E. Greene et al. 2024; K. N. Hainline et al. 2025). The compactness of these five objects, defined as the flux ratio between the $0.^{\circ}5$ and $0.^{\circ}2$ diameter apertures in the F444W filter, ranges from $1.5 - 1.8$, which is also similar to LRDs (J. E. Greene et al. 2024; K. N. Hainline et al. 2025). Although the physical nature of LRDs remains unclear, a large fraction of LRDs are found to feature AGN activity and SEDs that cannot be fitted by typical stellar templates. To ensure the purity of our sample

and consistency of our analyses, we exclude these five objects from the following analyses, resulting in a total of 161 objects in our sample.

As discussed earlier in this section, we use the $p(z)$ from **EAZY** as the priors of redshifts in **Prospector** SED fitting when z_{spec} is not available. Here we compare the performance of photometric redshift determination of **Prospector** and **EAZY** using the 14 galaxies at $z > 7$ with confirmed z_{spec} (Section 2). To perform such comparison, we run our standard SED fitting procedures mentioned earlier in this section on these 14 objects instead of fixing their redshifts to z_{spec} . The resulting photometric redshifts (z_{Prospect}) are compared with z_{spec} in the bottom panel of Figure 1. The z_{Prospect} of these 14 objects are in good agreement with their z_{spec} , with the $\sigma_{\text{MAE}} = 0.225$ and $\sigma_{\text{NMAD}} = 0.013$ statistics substantially improved compared with the **EAZY** fitting results.

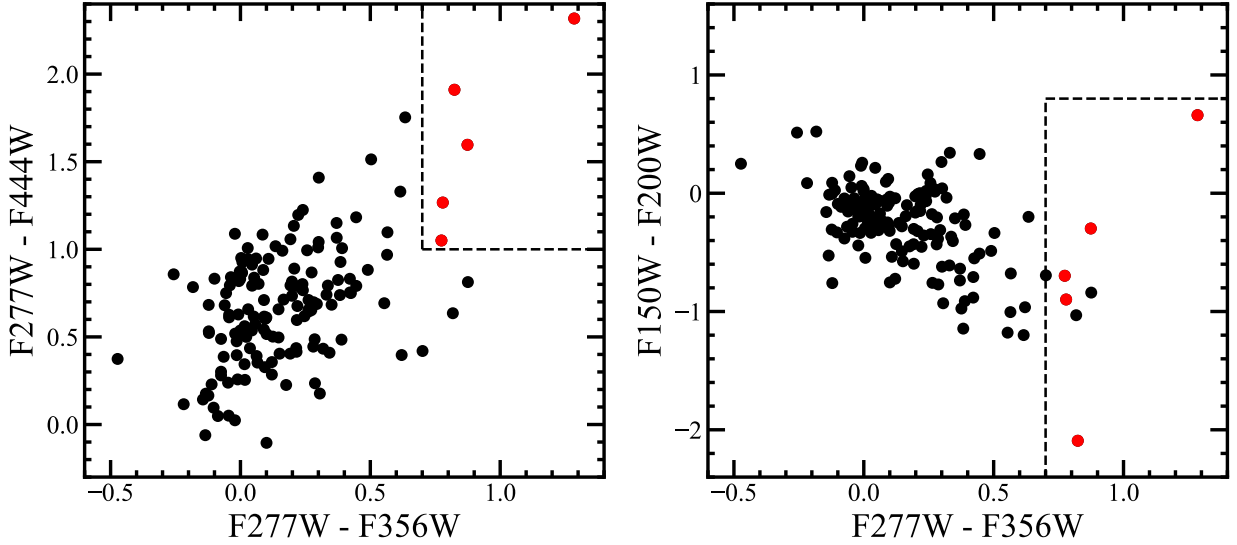


Figure 3. Rest-frame UV and optical colors of our galaxy candidates at $z > 7$ selected in Section 3. Red data points denote the five objects that are excluded due to their red optical color. The black dashed lines indicates the “little red dot” (LRD) selection criteria from J. E. Greene et al. (2024) and K. N. Hainline et al. (2025).

5. GALAXY PROPERTIES

In this section, we present the properties of our 161 galaxy candidates derived from multiband photometry and SED fitting (Section 4).

5.1. UV Continuum Properties

We measure UV continuum properties, including the absolute UV magnitude (M_{UV}) and the UV continuum slopes (β_{UV}) by fitting a power law (i.e., $f_{\lambda} \propto \lambda^{\beta}$) to the NIRCam photometry covering the rest-frame UV. The filter sets adopted for UV continuum measurements are based on the z_{phot} obtained in Section 4 and are selected to avoid potential Ly α contamination. For objects with $7.3 \lesssim z_{\text{phot}} \lesssim 9.7$ (F090W-dropouts), we use all the available filters including F150W, F200W, and F277W. For objects with $9.7 \lesssim z_{\text{phot}} \lesssim 13$ (F115W-dropouts), we use all the available filters including F200W, F277W, and F356W. For all 161 objects in our final sample, there are at least two filters used for UV continuum measurements. For each galaxy, we measure M_{UV} and β_{UV} with a Monte Carlo simulation, randomly drawing 200 realizations based on the measured values and errors of photometry and z_{phot} . Figure 4 shows the distribution of our galaxy candidates in the redshift- M_{UV} plane. Our sample covers a wide range of UV magnitude, spanning $M_{\text{UV}} = -17 \sim -22$. Noticeably, at $z = 13.7$, our single F150W-dropout galaxy has a bright UV luminosity of $M_{\text{UV}} = -21.2$, more luminous than any spectroscopically confirmed galaxy currently known at $z > 12$. The

detailed physical properties of this object will be discussed in 7.1.

In the left panel of Figure 5, we show the $M_{\text{UV}} - \beta_{\text{UV}}$ relation of our sample, together with the median and inner 68 percentiles β_{UV} in different M_{UV} bins. The β_{UV} of our sample has (16, 50, 84)-percentile values of $(-2.61, -2.21, -1.75)$, with the majority ($\gtrsim 70\%$) located at $\beta_{\text{UV}} < -2.0$. There are four galaxies in our sample with extremely blue UV continuum slopes characterized by $\beta_{\text{UV}} < -2.6$ even accounting for their measurement uncertainties. Such extremely blue galaxies, which have been reported to have low M_{*} and high sSFR (e.g., M. W. Topping et al. 2024; H. Yanagisawa et al. 2024), are suspected to have large ionizing photon escape fractions (f_{esc}). Due to the small number of such galaxies in our sample, we do not find strong correlation between extremely blue β_{UV} and M_{*} or sSFR.

To investigate this (non-)correlation, we fit our measurements with a linear relation $\beta_{\text{UV}} = \frac{d\beta}{dM_{\text{UV}}} M_{\text{UV}}^{-19} + \beta_0$ with an intrinsic scatter of $\sigma_{\beta, \text{UV}}$. Here $M_{\text{UV}}^{-19} \equiv M_{\text{UV}} + 19$, and β_0 represents the β_{UV} at $M_{\text{UV}} = -19$. We obtain the best-fit parameters $(\frac{d\beta}{dM_{\text{UV}}}, \beta_0, \sigma_{\beta, \text{UV}})$ with `emcee`, incorporating the measurement uncertainties of β_{UV} and M_{UV} . The derived relation, which is shown with the green solid line in the left panel of Figure 5, has the functional form of $\beta_{\text{UV}} = -0.01^{+0.04}_{-0.03} M_{\text{UV}}^{-19} - 2.19^{+0.04}_{-0.03}$ with an intrinsic scatter of $\sigma_{\beta, \text{UV}} = 0.29^{+0.02}_{-0.02}$. The best-fit slope, $\frac{d\beta_{\text{UV}}}{dM_{\text{UV}}} = -0.01^{+0.04}_{-0.03}$, indicates that there is no correlation between β_{UV} and M_{UV} , and is

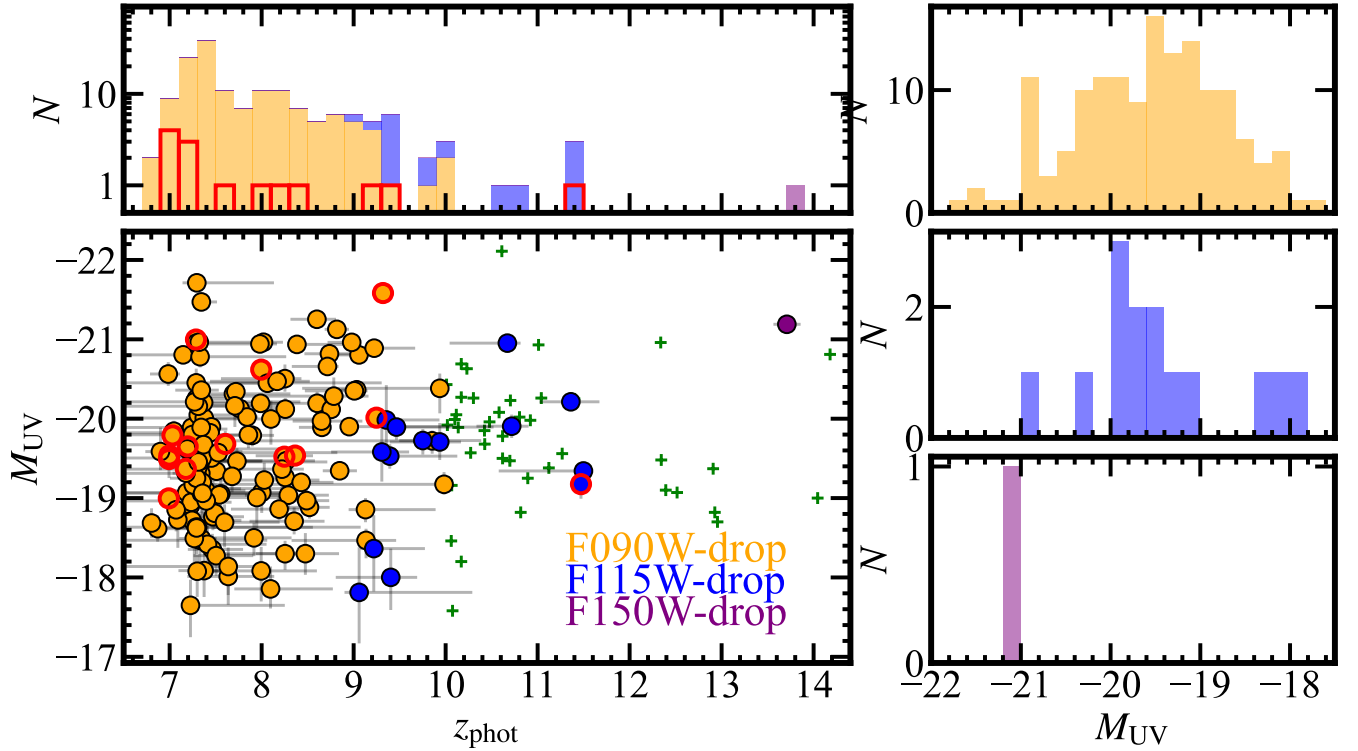


Figure 4. Left: histogram of z_{phot} distribution (top) and M_{UV} versus z_{phot} (bottom) for our sample. Objects with spectroscopic confirmation are marked with open red symbols and the red histogram. We also plot other spectroscopically confirmed galaxies at $z > 10$ in the literature with green data points. Right: histograms of M_{UV} distributions for the F090 (top), F115 (middle), and F150W (bottom) -dropout galaxies.

in agreement with the results $\frac{d\beta_{\text{UV}}}{dM_{\text{UV}}} = -0.06^{+0.05}_{-0.05}$ obtained from the JADES survey by M. W. Topping et al. (2024) at $z > 8$. Similarly, M. Franco et al. (2025) also found a flat slope of $\frac{d\beta_{\text{UV}}}{dM_{\text{UV}}} = -0.03^{+0.03}_{-0.03}$. Our best-fit $\beta_0 = -2.19^{+0.04}_{-0.03}$ is slightly redder than the value $-2.33^{+0.05}_{-0.05}$ reported in M. W. Topping et al. (2024), but is within the error when taking into account the intrinsic scatter $\sigma_{\beta,\text{UV}} = 0.31^{+0.02}_{-0.02}$.

For the $M_* - \beta_{\text{UV}}$ relation, we conduct similar analyses and present our results in the right panel of Figure 5. The $M_* - \beta_{\text{UV}}$ relation of our sample is best described by a linear function of $\beta_{\text{UV}} = 0.42^{+0.04}_{-0.05} \log(M_*/M_{\odot}) - 5.96^{+0.37}_{-0.34}$ with an intrinsic scatter of $\sigma_{\beta,\text{UV}} = 0.17^{+0.02}_{-0.02}$. The positive correlation is significant at the $> 3\sigma$ level, consistent with previous studies at $z = 4 - 8$ (S. L. Finkelstein et al. 2012) and $z = 9 - 11$ (S. Tacchella et al. 2022), indicates that more massive galaxies are redder in rest-UV color, and hence are likely more dusty or composed of older stellar populations.

Overall, our UV continuum analyses suggest that the $M_{\text{UV}} - \beta_{\text{UV}}$ and $M_* - \beta_{\text{UV}}$ relations of our sample do not

deviate from those previously reported in legacy fields at the similar redshifts.

5.2. Galaxy Main Sequence

We derive the SFR of our galaxies based on the rest-frame UV luminosity (L_{UV}) inferred from photometry. The UV luminosity is corrected for the dust attenuation (A_{1600}) that is estimated from the β_{UV} and the following relation (G. R. Meurer et al. 1999):

$$A_{\text{UV}} = 4.43 + 1.99\beta_{\text{UV}}. \quad (3)$$

The attenuation corrected L_{UV} is then converted to the UV SFR (R. C. Kennicutt 1998):

$$\text{SFR}_{\text{UV}} [M_{\odot} \text{ yr}^{-1}] = 1.4 \times 10^{-28} L_{\text{UV}} [\text{erg s}^{-1} \text{ Hz}^{-1}], \quad (4)$$

which is multiplied by 0.63 to account for the conversion from E. E. Salpeter (1955) IMF to G. Chabrier (2003) IMF (P. Madau & M. Dickinson 2014). We adopt the UV-based SFR measurements instead of directly using the SFR from SED fitting results because it is difficult to

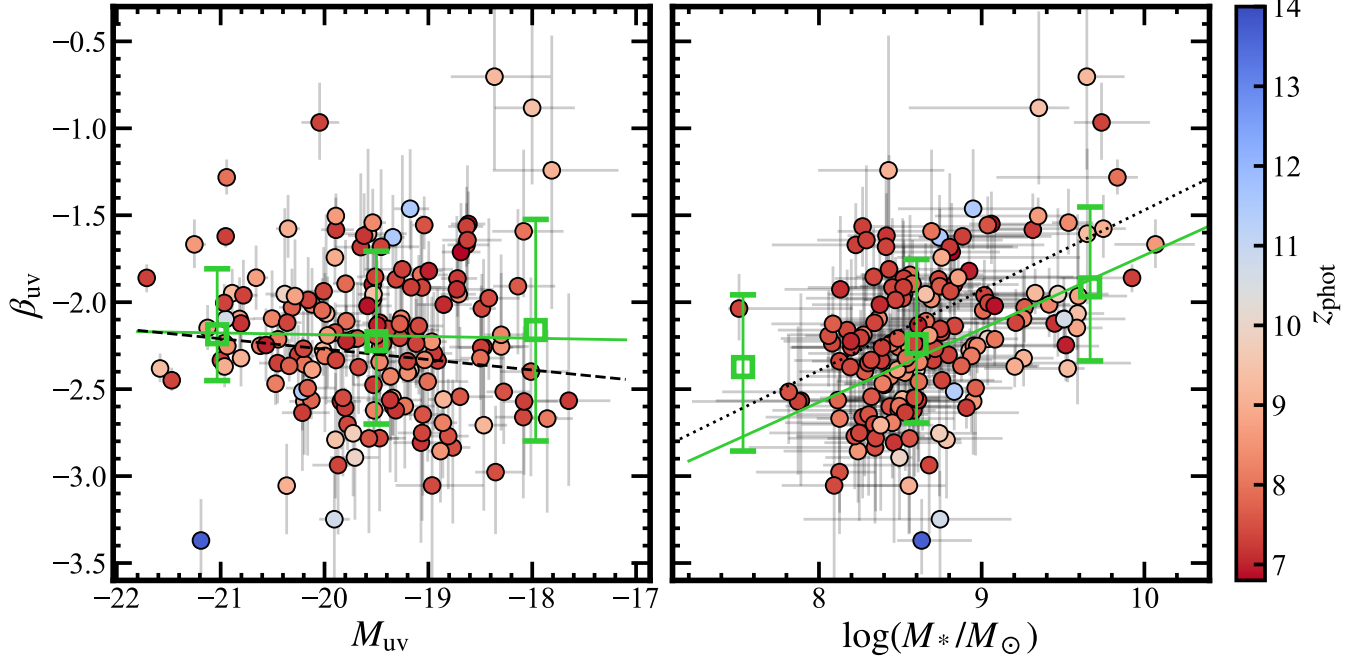


Figure 5. Left: β_{UV} versus M_{UV} for our sample of 161 $z \geq 7$ galaxies, where the data points are color-coded by redshift. The median β_{UV} and its inner 68 percentile distribution in different M_* bins are denoted with green open squares and error bars. The green solid line indicates our best-fit $M_{\text{UV}} - \beta_{\text{UV}}$ linear relation. The black dashed line shows the $M_{\text{UV}} - \beta_{\text{UV}}$ relation from M. W. Topping et al. (2024). Right: same as the left panel, but for β_{UV} versus M_* . The black dotted line shows the $M_* - \beta_{\text{UV}}$ relation from S. L. Finkelstein et al. (2012).

distinguish the detailed star forming history and other effects (e.g., dust attenuation, metallicity) of galaxies at $z > 7$ with the current observational datasets (e.g., S. Tacchella et al. 2022).

We present the galaxy main sequence (M_* –SFR relation) of our sample in Figure 6. We fit a line to the observed main sequence with $\log(\text{SFR}) = \alpha \log(M_*/M_0) + \beta$ with an intrinsic scatter of σ_{ms} , where $M_0 = 10^8 M_{\odot}$. Our best-fit result has a slope of $\alpha = 0.59^{+0.03}_{-0.04}$, a normalization of $\beta = 0.18^{+0.03}_{-0.03}$, and an intrinsic scatter of $\sigma_{\text{ms}} = 0.21^{+0.02}_{-0.02}$. In Figure 6, we also compare our result with other studies based on JWST-selected galaxies at the similar redshift. Overall, our best-fit main sequence is located between T. Morishita et al. (2024) and G. Roberts-Borsani et al. (2024), and is in good agreement with L. Clarke et al. (2025).

6. GALAXY SIZES

We estimate the sizes of galaxies with **Galfit** (C. Y. Peng et al. 2002, 2010), assuming a single simple surface brightness profile. Following T. Morishita et al. (2024), we fix the Sérsic index n to 1, i.e., a pure exponential law. For each galaxy, we first generate image cutouts (41 × 41 pixels in size, corresponding to $10''$) of the non-PSF-matched science, rms, and segmentation maps. We then mask out the neighboring sources us-

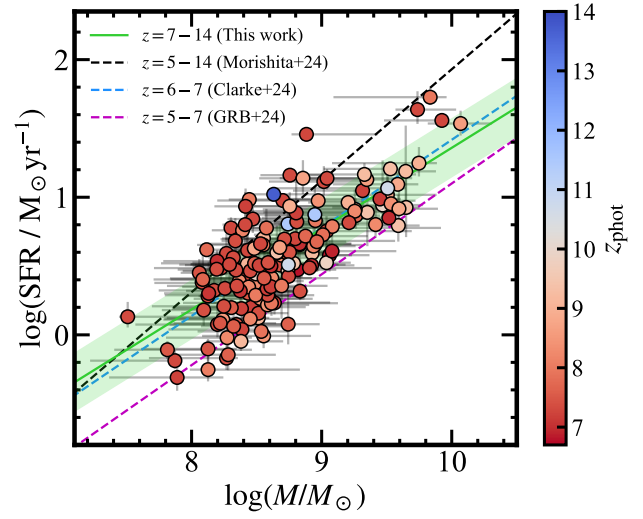


Figure 6. The M_* –SFR relation of our galaxy sample. Data points are color-coded in the same manner as Figure 5. The green line and shaded regions indicate the best-fit $\text{SFR} = \alpha \log(M_*/M_0) + \beta$ relation and the intrinsic scatter, respectively. The black, blue, and magenta dashed lines denote previous results from T. Morishita et al. (2024), L. Clarke et al. (2025), and G. Roberts-Borsani et al. (2024), respectively, at the similar redshift.

ing the segmentation map. We construct the empirical PSF models by selecting and stacking bright stars in the same field. For each galaxy, we perform the fit in the filter covering the rest-frame UV wavelengths, i.e., F150W(F200W) for F090W(F115W)-dropouts, obtaining the best-fit model and the corresponding effective radius (R_e), which is defined as the radius where 50% of the total flux is covered.

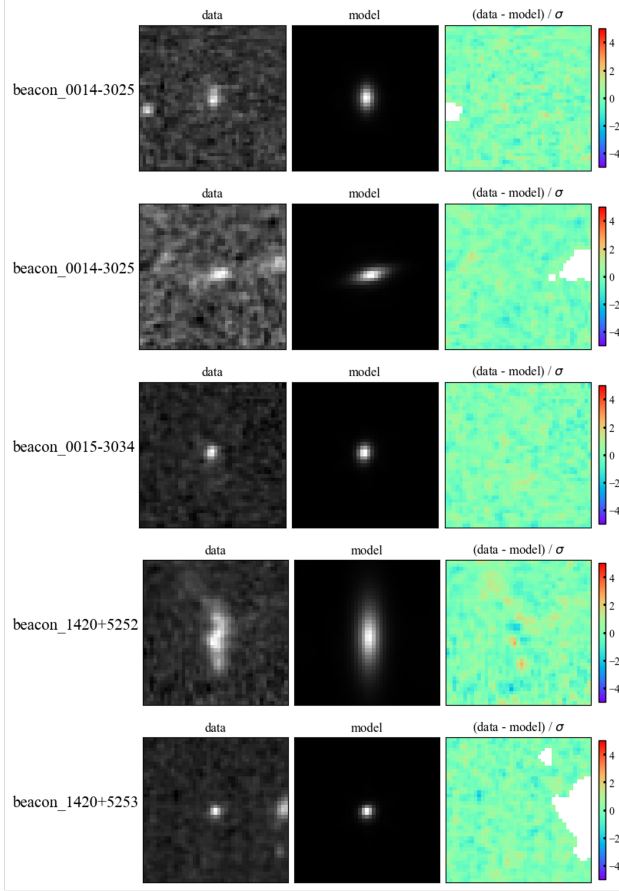


Figure 7. Examples of `galfit` fitting results. The left, middle, and right columns show the cutout images of galaxies, best-fit Sérsic profiles, and normalized residuals, respectively. Other sources are masked out in the last column.

After obtaining the best-fit results for each galaxy, we conduct visual inspections on the residual images, identifying 13 objects with significant residuals, e.g., objects with multiple clumps or interacting with neighboring galaxies. These 13 objects are excluded from the following galaxy size analyses.

Figure 7 shows examples of our `Galfit` fitting results. Overall, there are 14 galaxies with upper limit of $R_e=0.5$ pix (~ 57 pc at $z=7$). The sizes of our $z > 7$ galaxies range from compact values of $\lesssim 63$ pc to large values of ~ 1.28 kpc, with a median and inner 68 per-

centile values of $R_e = 310^{+320}_{-160}$ pc. In Figure 8, we show the histogram of the size distribution in natural logarithmic scale following the literature.

We fit the galaxy size distribution with a log-normal function:

$$p(R_e) dR_e = \frac{1}{2\pi\sigma_{\ln R_e}} \exp\left(\frac{[\ln(R_e/\bar{R}_e)]^2}{2\sigma_{\ln R_e}^2}\right) \frac{dR_e}{R_e}, \quad (5)$$

where \bar{R}_e and $\sigma_{\ln R_e}$ represent the R_e value at the peak and standard deviation of the distribution, respectively. To account for the measurement uncertainties, we randomly draw 100 realizations based on the measured R_e and the errors, repeating the fitting procedure. We obtain the best-fit median and inner 68 percentile $\bar{R}_e = 0.245^{+0.004}_{-0.004}$ kpc and $\sigma_{\ln R_e} = 0.96^{+0.04}_{-0.04}$. These values are broadly consistent with the results from Y. Ono et al. (2024, 2025), who measured the galaxy sizes at $z = 4 - 16$ in legacy fields with CEERS and JADES data. To test the robustness of our results, we repeat the analysis with n fixed to 1.5 and find that our conclusions remain unchanged, with the smallest resolved effective radius being $R_e = 73.6$ pc.

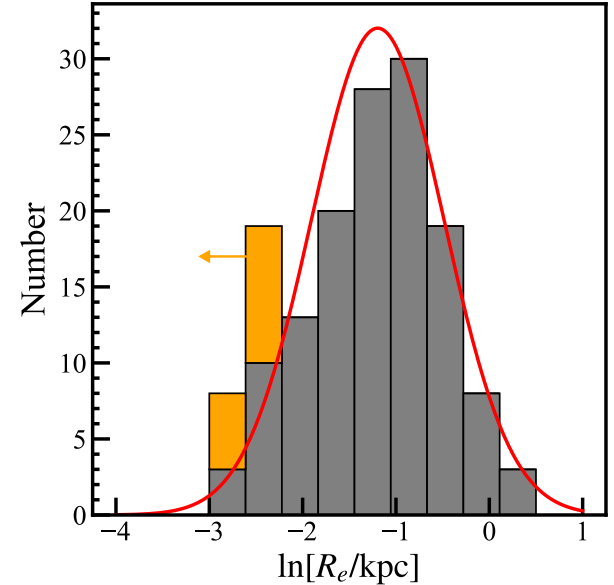


Figure 8. Histogram of R_e in natural logarithm scale. Measurements with upper limits are indicated with orange color. The red curve represents the best-fit log-normal distribution (see Section 6).

6.1. Size - Luminosity relation

We investigate the relation between size and luminosity of $z = 7 - 12$ galaxies. In Figure 9, we present the

$M_{\text{UV}} - R_e$ relation of our sample, together with the median and inner 68 percentile R_e in different M_{UV} bins. Following previous studies (e.g., T. Shibuya et al. 2015; Y. Ono et al. 2024), we attempted to fit a power-law function to the observed $M_{\text{UV}} - R_e$ relation:

$$R_e = R_0 \left(\frac{L_{\text{UV}}}{L_0} \right)^\alpha, \quad (6)$$

where R_0 is the effective radius at L_0 that corresponds to -21 Mag. We conduct the fitting in logarithm space following the fitting procedures in Section 5.1, obtaining the best-fit values of $R_0 = 0.34^{+0.04}_{-0.04}$ kpc, $\alpha = -0.05^{+0.03}_{-0.03}$, and a large intrinsic scatter in logarithm of 0.31 dex. For R_0 , our best-fit values are consistent with the results from Y. Ono et al. (2025) at the similar redshift. However, we do not find correlation between R_e and L_{UV} , given that our best-fit α is close to zero and the intrinsic scatter is large.

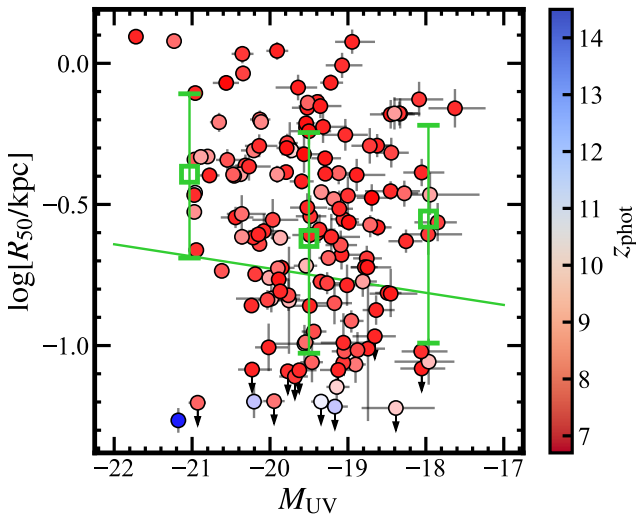


Figure 9. Size-luminosity relation of our sample. All symbols and colors are the same as those in Figure 5.

Next, we derive the SFR surface density (Σ_{SFR}) of our sample galaxies, which is estimated by:

$$\Sigma_{\text{SFR}} = \frac{0.5 \text{ SFR}}{\pi R_e^2}. \quad (7)$$

In Figure 10, we show the relation between M_* and Σ_{SFR} of our $z = 7 - 14$ galaxy sample. Similar to previous JWST results (e.g., A. Calabro et al. 2024; T. Morishita et al. 2024), our sample features a wide range of Σ_{SFR} spanning $0.2 - 630 M_{\odot} \text{ yr}^{-1} \text{ kpc}^{-2}$ with a median value of $\Sigma_{\text{SFR}} = 6.6 M_{\odot} \text{ yr}^{-1} \text{ kpc}^{-2}$, including $\sim 20\%$ with a

large Σ_{SFR} of $\log[\Sigma_{\text{SFR}} / M_{\odot} \text{ yr}^{-1} \text{ kpc}^{-2}] > 1.5$. Interestingly, Figure 10 suggests that galaxies at higher redshift tend to have larger $\log \Sigma_{\text{SFR}}$, which is consistent with the observed increase of $\log \Sigma_{\text{SFR}}$ from $z = 4 - 8$ (e.g., A. Calabro et al. 2024). The 20% M_{UV} completeness limits for the F090W-, F115W-, and F150W-dropout galaxies are -19.4 , -19.8 , and -20.0 , respectively. These modest differences in detection thresholds would produce only a ~ 0.2 dex shift in Σ_{SFR} . Hence, the observed trend of increased Σ_{SFR} towards higher redshifts is unlikely to be driven by selection effects. $\log \Sigma_{\text{SFR}}$ has been shown to be related to the gas density of the interstellar medium (ISM; T. Jiang et al. 2019; N. A. Reddy et al. 2023), ionization properties (N. A. Reddy et al. 2022), galactic feedback efficiency (e.g., T. M. Heckman & S. Borthakur 2016; M. Llerena et al. 2023). The possible increase of $\log \Sigma_{\text{SFR}}$ with redshift could result from denser environments, harder ionization, or varying outflow efficiency towards higher redshift.

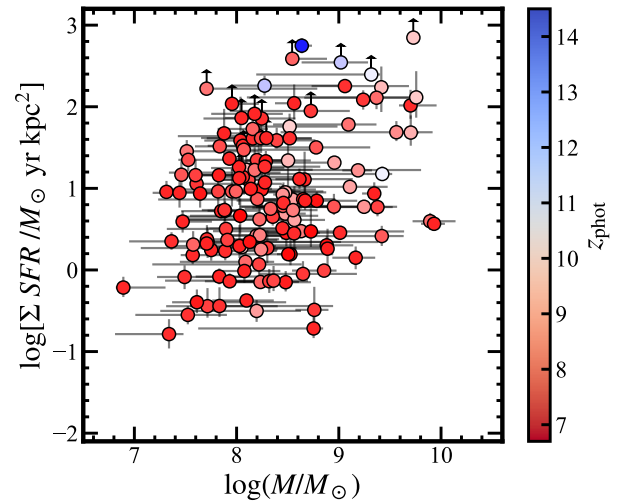


Figure 10. The $\Sigma_{\text{SFR}} - M_*$ relation of our sample. The symbols and colors are the same as those in Figure 5.

7. DISCUSSION

7.1. A Remarkably Bright, Compact Star-forming galaxy at $z = 14$

In Section 3, we identified one F-150W dropout galaxy candidate, beacon_1420+5253.4770, at $z = 13.7$ with an extremely bright UV luminosity of $M_{\text{UV}} = -21.2$. As shown in Figure 4, if spectroscopically confirmed, it would be the brightest galaxy at $z > 12$. Located in the EGS field, this object was also identified by A. Weibel et al. (2025) as ID89475. BEACON DR2 has one of

Table 2. Physical Properties of beacon_1420+5253_4770

z_{EAZY}	$13.52^{+0.15}_{-0.14}$
z_{Prospect}	$13.71^{+0.15}_{-0.15}$
M_{UV}	$-21.19^{+0.08}_{-0.08}$
β_{UV} (photometry)	$-3.37^{+0.24}_{-0.19}$
$\log(M_{*}/M_{\odot})$	$8.63^{+0.31}_{-0.15}$
SFR (UV)	$10.51^{+0.58}_{-0.68} M_{\odot} \text{ yr}^{-1}$
R_e (UV)	$55.3^{+5.6}_{-5.6} \text{ pc}$
Σ_{SFR} (UV)	$547.4^{+114.6}_{-116.1} M_{\odot} \text{ yr}^{-1} \text{ kpc}^{-2}$

the most filter coverages in this field with 16 broad and medium band filters, providing strong constraints for SED fitting. As presented in Figure 11, beacon_1420-5253_4770 is not detected in F140M and bluer filters. While there may be signals observed in the F150W filter, the detection is only at $S/N = 1.5$. There is a clear break observed in the F182M filter with $S/N = 7.8$, tightly constraining the photometric redshift of the object.

The properties derived from BEACON DR2 photometry and SED fitting are summarized in Table 2. The galaxy exhibits a compact yet resolved morphology with an effective radius of $R_e = 55.3 \pm 5.6$ pc, indicative of compact star formation with a high Σ_{SFR} of $547.4^{+114.6}_{-116.1} M_{\odot} \text{ yr}^{-1} \text{ kpc}^{-2}$. However, the potential contribution from an AGN cannot be ruled out. The β_{UV} inferred from the photometry is remarkably blue, $-3.37^{+0.24}_{-0.19}$, likely induced by the high flux in the F277W filter. If the measured β_{UV} is true, beacon_1420-5253_4770 might have extremely low metallicity or high ionizing photon escape fraction with a weak nebular continuum (e.g., H. Yanagisawa et al. 2024; M. W. Topping et al. 2024). Alternatively, if the measured β_{UV} is affected by strong nebular emission lines (e.g., HeII) in the F277W filter, this would imply the presence of powerful ionizing sources. Metal-poor stars, again, could explain such a scenario, while the existence of AGN remains another possibility. Future spectroscopic follow-up would help confirm the nature of beacon_1420+5253_4770.

7.2. Galaxy Overdensities

One key advantage of wide-area, pure-parallel surveys such as BEACON is their ability to sample the universe through independent pointings, enabling robust identification of galaxy clustering. In this subsection, we identify and characterize the galaxy overdensities from the 36 BEACON DR2 pointings.

Following the methodology of M. Trenti et al. (2012), as detailed in K. C. Kreilgaard et al. (in preparation), we evaluate the statistical significance of an overdense field by computing the Poisson probability of observing N_{obs} or more galaxies in a pointing within a cer-

tain redshift window where N_{exp} are expected, $P(N \geq N_{\text{obs}} | N_{\text{exp}})$. Within each search volume, we obtain N_{obs} by counting the galaxies whose best-fit **EAZY** photometric redshifts, evaluated at the peak of $p(z)$, fall within the redshift window. The **EAZY** photometric redshift is chosen over the **Prospector** results to maintain consistency with the simulations used to derive N_{exp} . We calculate N_{exp} by integrating the UV luminosity functions (LFs) derived from the same BEACON DR2 dataset across 36 pointings (K. C. Kreilgaard et al., in preparation) over the relevant redshift interval. The integration limit in M_{UV} is set by the faintest member galaxy identified in each search volume, which varies among different pointings and redshift windows and may fall below the 100% detection completeness. However, such an effect is incorporated in the N_{exp} estimation through the simulated completeness function and thus the UV LF determination. Given the 100% purity of our sample selection (Section 3), we do not consider contamination in our N_{exp} estimation.

We search for overdensities with the redshift window of $\delta z = 0.6$. This large range is chosen to match the accuracy of the **EAZY** photometric redshift in Section 3 ($\sim 2\sigma_{\text{MAE}}$). We identify a field as an overdensity candidate if $P(N \geq N_{\text{obs}} | N_{\text{exp}}) < 0.003$, corresponding to a 3σ detection. To further account for the uncertainties in **EAZY** photometric redshifts, we also calculate the probability that all the member galaxies fall within δz window, P_{OD} , based on their $p(z)$ distributions. We require $P_{\text{OD}} > 0.5$ to classify an overdensity as a robust detection. With the $P(N \geq N_{\text{obs}} | N_{\text{exp}}) < 0.003$ and $P_{\text{OD}} > 0.5$ criteria, we identify three galaxy overdensity fields, listed in Table 3. In Figure 12, we show the sky distribution and the **EAZY** $p(z)$ of these fields. Below we briefly describe these three fields:

beacon_0015-3034 This overdense field is close to the ABELL-2744 field, where a $z = 7.88$ protocluster has been spectroscopically confirmed (e.g., T. Morishita et al. 2025b). However, no spectroscopically confirmed galaxies are found in our BEACON pointing. The field also lacks bright galaxies with $M_{\text{UV}} < 20.5$. Two galaxies exhibit relatively red UV continua with $\beta_{\text{UV}} > -1.7$.

beacon_1420+5252 Located within EGS field, this overdense region partially overlaps with a $z = 7.3$ protocluster spectroscopically identified by Z. Chen et al. (2025), with 2/10 of our member galaxies included in their sample. The field contains two bright galaxies with $M_{\text{UV}} < 20.5$, which may be associated with the large ionizing bubbles identified in the EGS field (e.g., M. Tang et al. 2023; Z. Chen et al. 2025). One of the two bright galaxies has a relatively large stellar mass of $\log(M_{*}/M_{\odot}) > 9.5$. There are another two red galaxies

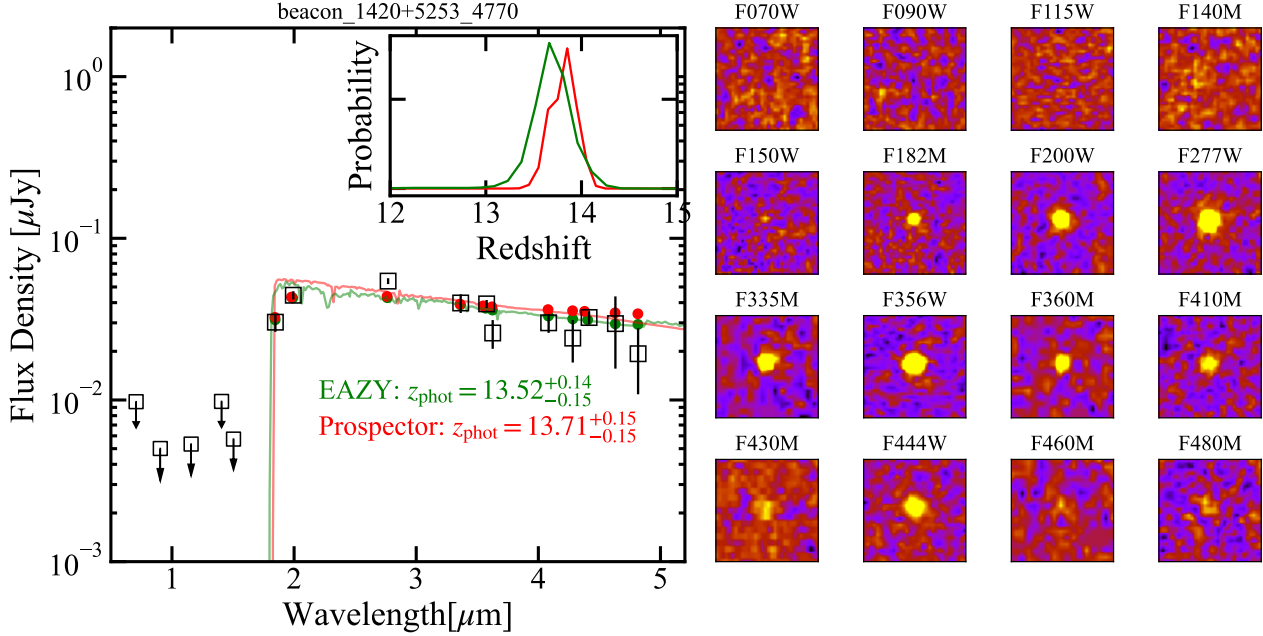


Figure 11. Left: The best-fit **EAZY** (green) and **Prospector** (red) SEDs of `beacon_1420+5253_4770`, a candidate of brightest galaxy at $z > 12$. The observed photometry is shown with black open squares with error bars. The photometry predicted from the best-fit SEDs is denoted with solid circles. The inset figure presents the $p(z)$ of the SED fitting results. Right: $1'' \times 1''$ image stamps of `beacon_1420+5253_4770`.

Table 3. Summary of the three galaxy overdensity fields found in BEACON DR2

Field	n	δ	z_{med}
<code>beacon_0015-3034</code>	7	13.4	7.18
<code>beacon_1420+5252</code>	10	26.9	7.17
<code>beacon_2325-1203</code>	7	12.9	7.38

with $\beta_{\text{UV}} > -1.7$, suggesting a comparatively evolved environment in this overdense field.

`beacon_2325-1203` This field is in a previously unexplored extragalactic region, with BEACON providing the first photometric data coverage. The field contains one bright galaxy with $M_{\text{UV}} < 20.5$, but no galaxies having red UV continua or large stellar masses ($\log(M_*/M_{\odot}) > 9.5$).

To explore how galaxy properties vary with environment at $z > 7$, we divide our galaxy sample into two subsets, the 24 galaxies in overdense fields listed in Table 3 (hereafter “overdense galaxies”) and those outside these regions (hereafter “field galaxies”). To make a fair comparison, we limit the field galaxy sample to F090-dropout galaxies. The total number of field galaxies is

$151 - 24 = 127$. In Figure 13, we present the normalized histograms of physical properties, including $M_{\text{UV}}, \beta_{\text{UV}}, M_*, \text{SFR}$, galaxy distance to the main sequence (ΔMS , Figure 6), $\ln R_e$, and $\log \Sigma_{\text{SFR}}$, for overdense and field galaxies, with Poisson-based error bars. Histogram bin widths are chosen to exceed typical measurement uncertainties. The median and inner 68th percentile of each distribution are indicated by vertical dashed lines and shaded regions, respectively. Visually, the ΔMS distribution for overdense galaxies appears slightly skewed toward higher values compared with field galaxies, although the medians of the two distributions remain consistent within statistical uncertainties. For all other properties, the distributions of overdense and field galaxies appear consistent.

To quantitatively assess these differences, we perform two-sample Kolmogorov–Smirnov (KS) tests, incorporating measurement uncertainties through 500 Monte Carlo realizations, and report the median and inner 68th percentile of the resulting p -value distributions in Figure 13. We find that the median p -values for all examined properties are well above 0.05 (corresponding to a 2σ significance threshold), indicating that none of the parameters show statistically significant differences between overdense and field galaxies.

In a previous JWST study, Q. Li et al. (2025) investigated the dependence of galaxies properties on envi-

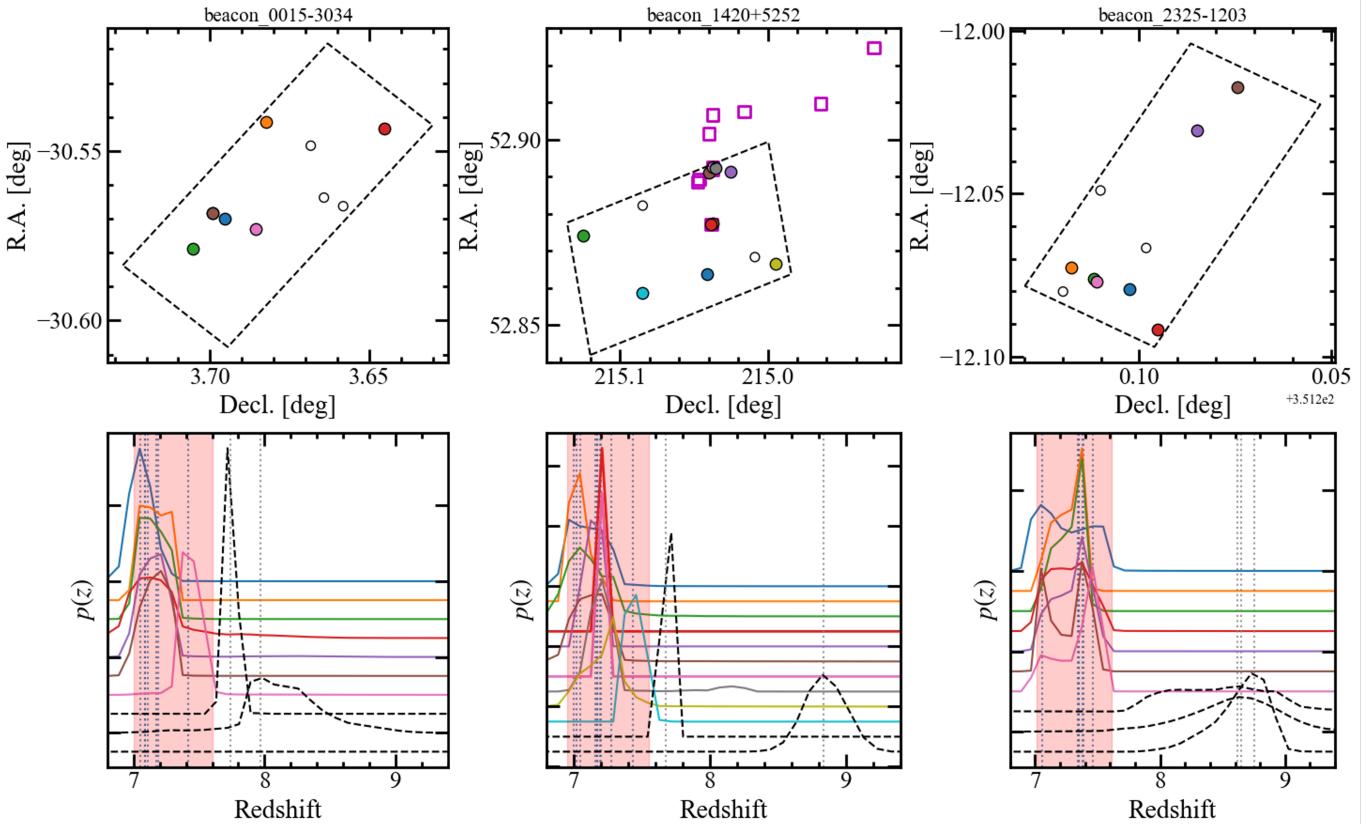


Figure 12. The projected sky distribution (top) and $p(z)$ (bottom) of the three overdense fields identified in BEACON DR2. In the top row, the objects outside our δz window are shown with open black points, while the NIRCam field of view (FoV) is indicated with black dashed boxes. For beacon_1420+5252 in EGS field, the member galaxies of the $z = 7.2$ overdensity in Z. Chen et al. (2025) are indicated with magenta open squares. In the bottom row, the colors of $p(z)$ distributions match the colors of data points in the top row, except for galaxies outside the δz window that are shown with black dashed curves. The red shaded regions indicate the δz windows for identifying these overdensities.

ronment based on 26 overdensities at $z < 7$, finding that overdense galaxies may experience accelerated star formation and dust enrichment as indicated by higher specific SFR (sSFR) and redder β_{UV} , respectively. In contrast, we do not find such trends in Figure 13. This difference might arises because our analyses focus on a slightly higher redshift regime at $z > 7$, where the Universe is younger than 800 Myr. Although elevated sSFRs and/or redder β_{UV} have been reported in individual extreme overdensities at $z > 7$ (e.g., K. Daikuhara et al. 2025; C. Witten et al. 2025), our results based on 35 independent BEACON DR2 pointings suggest such environmental effects may not be widespread until later cosmic epochs.

Another plausible explanation for the lack of a detected dependence of sSFR (or ΔMS) on environment is the limited sample size. To assess the statistical power of our data, we perform simulations to determine the sample size required to detect a difference in the ΔMS distributions between overdense and field galaxies. As-

suming that the underlying distributions of M_* and SFR is identical to the current sample, we generate bootstrap realizations in which the numbers of overdense and field galaxies are increased by a factor of N , and repeat the same analysis. We find that with $10\times$ more galaxies, the difference in ΔMS between overdense and field galaxies would be recovered with a median p -value of 0.017 ($\sim 2.4\sigma$), highlighting the need for future pure-parallel observations. Future spectroscopic follow-up observations would also help improve the measurement uncertainties and provide constraints on the environmental effects of various galaxy physical parameters.

8. SUMMARY

In this work, we present the analysis of 161 robust galaxy candidates at $z = 7 - 14$ selected from 36 independent pointings (corresponding to $\sim 350 \text{ arcmin}^2$) in the second data release (DR2) of BEACON, a JWST Cycle 2 pure-parallel NIRCam imaging program. We estimate the properties, including z_{phot} and M_* , of our

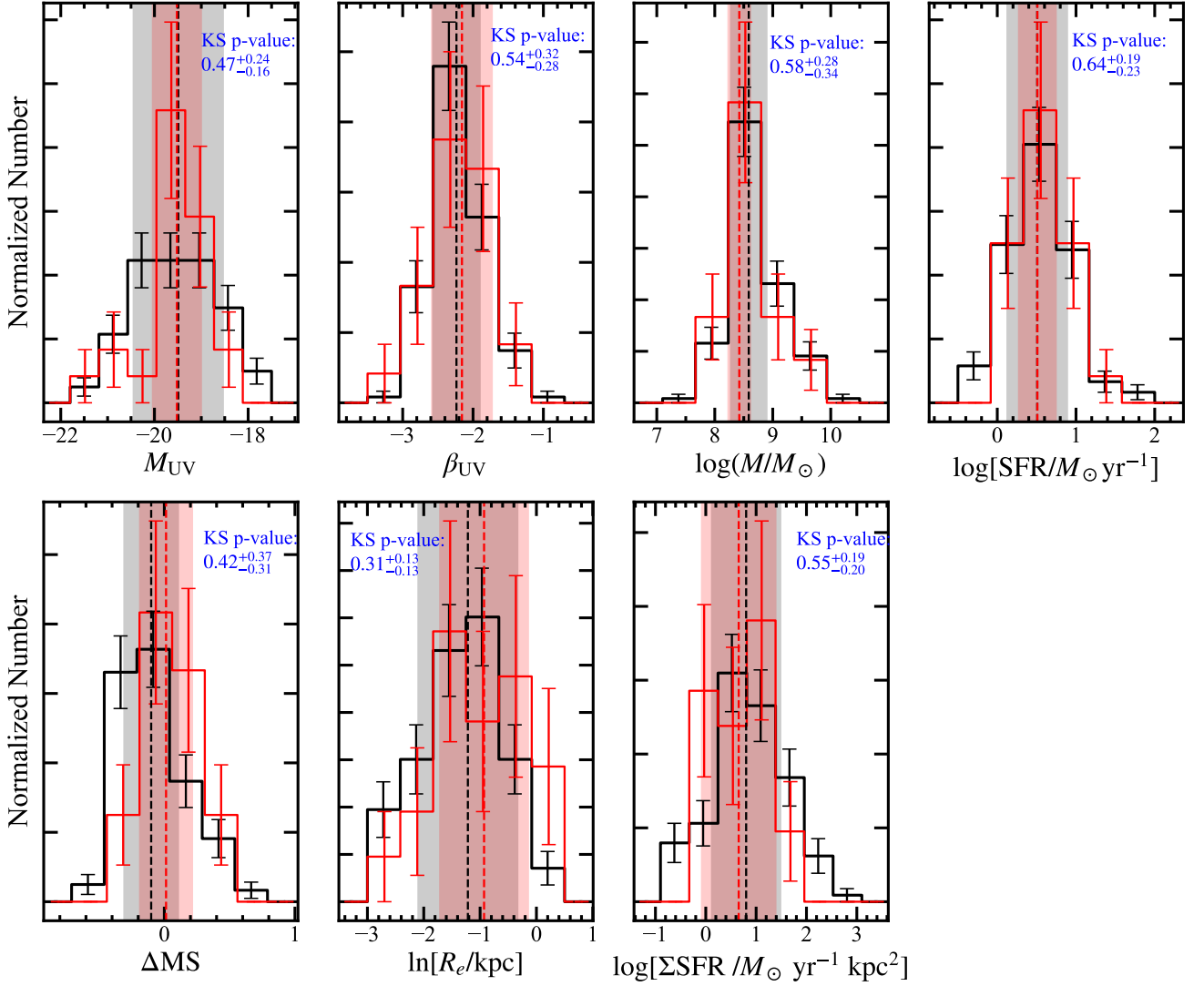


Figure 13. Normalized histograms of M_{UV} , β_{UV} , M_* , SFR, sSFR, $\ln R_e$, and $\log \Sigma_{\text{SFR}}$ of our galaxy sample in overdensities (red) and the field (black), with vertical bars indicating the Poisson errors. We perform the two-sample KS test on 100 Monte Carlo realizations of each physical parameter, and report the median and inner 68 percentile distribution of the p-values at the top of each panel (See Section 7.2).

sample based on SED fitting using **Prospector**, utilizing the redshift probability distribution obtained from **EAZY**. Our sample contains 14 spectroscopically confirmed sources, among which the z_{phot} errors, defined as $|z_{\text{phot}} - z_{\text{spec}}|/(1 + z_{\text{spec}})$, are smaller than 10%. Out of the 161 objects, 146 are selected as F090W-dropout galaxies ($7.3 \lesssim z \lesssim 9.7$), 14 as F115W-dropout galaxies ($9.7 \lesssim z \lesssim 13$), and one as a F150W- dropout galaxy ($13 \lesssim z \lesssim 18$).

Combining our SED analysis with multi-band photometry, we characterize the key physical properties of our sample, including M_{UV} , β_{UV} , M_* , and SFR. The UV luminosity functions and clustering properties will

be presented in the accompanying paper (Kreilgaard et al. in preparation). We find no correlation between β_{UV} and M_{UV} , whose linear correlation has a slope of $\frac{d\beta_{\text{UV}}}{dM_{\text{UV}}} = -0.01^{+0.04}_{-0.04}$. In contrast, the $\beta_{\text{UV}} - M_*$ relation has a linear slope of $\frac{d\beta_{\text{UV}}}{dM_*} = 0.27^{+0.04}_{-0.04}$. The $M_* - \text{SFR}$ main sequence of our sample is consistent with previous measurements at the similar redshift (L. Clarke et al. 2025; T. Morishita et al. 2024; G. Roberts-Borsani et al. 2024), suggesting no differences between the results from pure-parallal and legacy fields.

We analyzed the rest-frame UV morphology of our galaxies with NIRCam imaging data. Assuming $n = 1$ Sérsic profiles, the sizes of our galaxies span $R_e =$

0.063 – 1.28 kpc, and can be described by a log-normal distribution that peaks at $\overline{R_e} = 0.245^{+0.004}_{-0.004}$ kpc with a standard distribution of $\sigma_{\ln R_e} = 0.96^{+0.04}_{-0.04}$.

We highlight the single F150W-dropout galaxy in our sample, beacon_1420+5253.4770, at $z = 13.7$ with $M_{\text{UV}} = -21.2$ that is brighter than any spectroscopically confirmed galaxies at $z > 12$. This galaxy has a compact but resolved morphology with $R_e = 55.3 \pm 5.6$ pc, a remarkably high Σ_{SFR} of $547.4^{+114.6}_{-116.3} M_{\odot} \text{ yr}^{-1} \text{ kpc}^{-2}$, and an extremely blue UV continuum of $\beta_{\text{UV}} = -3.37^{+0.24}_{-0.19}$ measured from photometry, suggesting that this object might have an extremely low metallicity, a high ionizing gas escape fraction, or contribution from AGN.

Utilizing the multiple independent sightlines of BEACON DR2, we identified three galaxy overdensity fields at $z = 7.0 - 7.5$ with $> 3\sigma$ significance levels. One of these fields, beacon_1420+5252, partially overlaps with a spectroscopically confirmed overdensity at $z = 7.2$ in EGS field (Z. Chen et al. 2025). The other two fields are newly identified in this study, showcasing the strength of pure-parallel imaging in identifying clustering of galaxies. We further investigate the dependence of different physical parameters on various environment, dividing our galaxies into those located in (“overdense galaxies”) and out of (“field galaxies”) the overdense fields. We find that there is no significant differences in the distributions of these parameters, suggesting that the accelerated star formation found in individual systems (e.g., C. Witten et al. 2025; K. Daikuhara et al. 2025) may not be widespread until later epochs (Q. Li et al. 2025). Alternatively, the absence of a detectable environmental dependence may simply reflect the limited sample size.

Our simulations indicate that an enhancement of SFR in overdense galaxies would be detected at a significance level exceeding 2σ if the current sample were increased by an order of magnitude. Future pure-parallel observations will therefore be crucial for probing the environmental dependence of galaxy properties at cosmic dawn.

ACKNOWLEDGMENTS

Support for program 3990 was provided by NASA through the Space Telescope Science Institute, which is operated by the Association of Universities for Research in Astronomy, Inc., under NASA contract NAS 5-03127. All of the data presented in this paper were obtained from the Mikulski Archive for Space Telescopes (MAST) at the Space Telescope Science Institute. Some of the data products presented herein were retrieved from the Dawn JWST Archive (DJA). DJA is an initiative of the Cosmic Dawn Center (DAWN), which is funded by the Danish National Research Foundation under grant DNRF140. MB acknowledges support from the ERC Grant FIRSTLIGHT and Slovenian national research agency ARIS through grants N1-0238 and P1-0188.

Facilities: JWST(NIRCam)

Software: astropy (Astropy Collaboration et al. 2013, 2018, 2022), EAZY (G. B. Brammer et al. 2008), Galfit (C. Y. Peng et al. 2002, 2010), Prospector (B. D. Johnson et al. 2021), Source Extractor (E. Bertin & S. Arnouts 1996)

REFERENCES

Adams, N. J., Conselice, C. J., Austin, D., et al. 2024, ApJ, 965, 169, doi: [10.3847/1538-4357/ad2a7b](https://doi.org/10.3847/1538-4357/ad2a7b)

Akins, H. B., Casey, C. M., Allen, N., et al. 2023, ApJ, 956, 61, doi: [10.3847/1538-4357/acef21](https://doi.org/10.3847/1538-4357/acef21)

Astropy Collaboration, Robitaille, T. P., Tollerud, E. J., et al. 2013, A&A, 558, A33, doi: [10.1051/0004-6361/201322068](https://doi.org/10.1051/0004-6361/201322068)

Astropy Collaboration, Price-Whelan, A. M., Sipőcz, B. M., et al. 2018, AJ, 156, 123, doi: [10.3847/1538-3881/aabc4f](https://doi.org/10.3847/1538-3881/aabc4f)

Astropy Collaboration, Price-Whelan, A. M., Lim, P. L., et al. 2022, ApJ, 935, 167, doi: [10.3847/1538-4357/ac7c74](https://doi.org/10.3847/1538-4357/ac7c74)

Barro, G., Pérez-González, P. G., Kocevski, D. D., et al. 2024, ApJ, 963, 128, doi: [10.3847/1538-4357/ad167e](https://doi.org/10.3847/1538-4357/ad167e)

Bertin, E., & Arnouts, S. 1996, A&AS, 117, 393, doi: [10.1051/aas:1996164](https://doi.org/10.1051/aas:1996164)

Boucaud, A., Bocchio, M., Abergel, A., et al. 2016, A&A, 596, A63, doi: [10.1051/0004-6361/201629080](https://doi.org/10.1051/0004-6361/201629080)

Bradley, L. 2023,, 1.1.0 Zenodo, doi: [10.5281/zenodo.10145563](https://doi.org/10.5281/zenodo.10145563)

Bradley, L. D., Trenti, M., Oesch, P. A., et al. 2012, ApJ, 760, 108, doi: [10.1088/0004-637X/760/2/108](https://doi.org/10.1088/0004-637X/760/2/108)

Brammer, G., Strait, V., Matharu, J., & Momcheva, I. 2022,, 1.5.0, Zenodo Zenodo, doi: [10.5281/zenodo.6672538](https://doi.org/10.5281/zenodo.6672538)

Brammer, G. B., van Dokkum, P. G., & Coppi, P. 2008, ApJ, 686, 1503, doi: [10.1086/591786](https://doi.org/10.1086/591786)

Calabro, A., Pentericci, L., Santini, P., et al. 2024, A&A, 690, A290, doi: [10.1051/0004-6361/202449768](https://doi.org/10.1051/0004-6361/202449768)

Cardelli, J. A., Clayton, G. C., & Mathis, J. S. 1989, ApJ, 345, 245, doi: [10.1086/167900](https://doi.org/10.1086/167900)

Carniani, S., Hainline, K., D'Eugenio, F., et al. 2024, *Nature*, 633, 318, doi: [10.1038/s41586-024-07860-9](https://doi.org/10.1038/s41586-024-07860-9)

Castellano, M., Fontana, A., Treu, T., et al. 2022, *ApJL*, 938, L15, doi: [10.3847/2041-8213/ac94d0](https://doi.org/10.3847/2041-8213/ac94d0)

Castellano, M., Fontana, A., Treu, T., et al. 2023, *ApJL*, 948, L14, doi: [10.3847/2041-8213/accea5](https://doi.org/10.3847/2041-8213/accea5)

Chabrier, G. 2003, *PASP*, 115, 763, doi: [10.1086/376392](https://doi.org/10.1086/376392)

Chen, Z., Stark, D. P., Mason, C. A., et al. 2025, arXiv e-prints, arXiv:2505.24080, doi: [10.48550/arXiv.2505.24080](https://doi.org/10.48550/arXiv.2505.24080)

Choi, J., Conroy, C., & Byler, N. 2017, *ApJ*, 838, 159, doi: [10.3847/1538-4357/aa679f](https://doi.org/10.3847/1538-4357/aa679f)

Choi, J., Dotter, A., Conroy, C., et al. 2016, *ApJ*, 823, 102, doi: [10.3847/0004-637X/823/2/102](https://doi.org/10.3847/0004-637X/823/2/102)

Clarke, L., Shapley, A. E., Lam, N., et al. 2025, arXiv e-prints, arXiv:2510.06681, doi: [10.48550/arXiv.2510.06681](https://doi.org/10.48550/arXiv.2510.06681)

Conroy, C., & Gunn, J. E. 2010, *ApJ*, 712, 833, doi: [10.1088/0004-637X/712/2/833](https://doi.org/10.1088/0004-637X/712/2/833)

Conroy, C., Gunn, J. E., & White, M. 2009, *ApJ*, 699, 486, doi: [10.1088/0004-637X/699/1/486](https://doi.org/10.1088/0004-637X/699/1/486)

Cueto, E. R., Hutter, A., Dayal, P., et al. 2024, *A&A*, 686, A138, doi: [10.1051/0004-6361/202349017](https://doi.org/10.1051/0004-6361/202349017)

Curtis-Lake, E., Carniani, S., Cameron, A., et al. 2023, *Nature Astronomy*, 7, 622, doi: [10.1038/s41550-023-01918-w](https://doi.org/10.1038/s41550-023-01918-w)

Daikuhara, K., Morishita, T., Kodama, T., et al. 2025, arXiv e-prints, arXiv:2507.13456, doi: [10.48550/arXiv.2507.13456](https://doi.org/10.48550/arXiv.2507.13456)

Dekel, A., Sarkar, K. C., Birnboim, Y., Mandelker, N., & Li, Z. 2023, *MNRAS*, 523, 3201, doi: [10.1093/mnras/stad1557](https://doi.org/10.1093/mnras/stad1557)

Ferrara, A. 2024, *A&A*, 684, A207, doi: [10.1051/0004-6361/202348321](https://doi.org/10.1051/0004-6361/202348321)

Ferrara, A., Carniani, S., di Mascia, F., et al. 2025a, *A&A*, 694, A215, doi: [10.1051/0004-6361/202452368](https://doi.org/10.1051/0004-6361/202452368)

Ferrara, A., Pallottini, A., & Dayal, P. 2023, *MNRAS*, 522, 3986, doi: [10.1093/mnras/stad1095](https://doi.org/10.1093/mnras/stad1095)

Ferrara, A., Pallottini, A., & Sommovigo, L. 2025b, *A&A*, 694, A286, doi: [10.1051/0004-6361/202452707](https://doi.org/10.1051/0004-6361/202452707)

Finkelstein, S. L., Papovich, C., Salmon, B., et al. 2012, *ApJ*, 756, 164, doi: [10.1088/0004-637X/756/2/164](https://doi.org/10.1088/0004-637X/756/2/164)

Finkelstein, S. L., Bagley, M. B., Ferguson, H. C., et al. 2023, *ApJL*, 946, L13, doi: [10.3847/2041-8213/acade4](https://doi.org/10.3847/2041-8213/acade4)

Fiore, F., Ferrara, A., Bischetti, M., Feruglio, C., & Travascio, A. 2023, *ApJL*, 943, L27, doi: [10.3847/2041-8213/acb5f2](https://doi.org/10.3847/2041-8213/acb5f2)

Franco, M., Casey, C. M., Akins, H. B., et al. 2025, arXiv e-prints, arXiv:2508.04791, doi: [10.48550/arXiv.2508.04791](https://doi.org/10.48550/arXiv.2508.04791)

Furtak, L. J., Zitrin, A., Plat, A., et al. 2023, *ApJ*, 952, 142, doi: [10.3847/1538-4357/acdc9d](https://doi.org/10.3847/1538-4357/acdc9d)

Gelli, V., Mason, C., & Hayward, C. C. 2024, *ApJ*, 975, 192, doi: [10.3847/1538-4357/ad7b36](https://doi.org/10.3847/1538-4357/ad7b36)

Gordon, K. D., Clayton, G. C., Misselt, K. A., Landolt, A. U., & Wolff, M. J. 2003, *ApJ*, 594, 279, doi: [10.1086/376774](https://doi.org/10.1086/376774)

Greene, J. E., Labbe, I., Goulding, A. D., et al. 2024, *ApJ*, 964, 39, doi: [10.3847/1538-4357/ad1ee5](https://doi.org/10.3847/1538-4357/ad1ee5)

Hainline, K. N., Johnson, B. D., Robertson, B., et al. 2024a, *ApJ*, 964, 71, doi: [10.3847/1538-4357/ad1ee4](https://doi.org/10.3847/1538-4357/ad1ee4)

Hainline, K. N., Helton, J. M., Johnson, B. D., et al. 2024b, *ApJ*, 964, 66, doi: [10.3847/1538-4357/ad20d1](https://doi.org/10.3847/1538-4357/ad20d1)

Hainline, K. N., Maiolino, R., Juodžbalis, I., et al. 2025, *ApJ*, 979, 138, doi: [10.3847/1538-4357/ad9920](https://doi.org/10.3847/1538-4357/ad9920)

Harikane, Y., Nakajima, K., Ouchi, M., et al. 2024, *ApJ*, 960, 56, doi: [10.3847/1538-4357/ad0b7e](https://doi.org/10.3847/1538-4357/ad0b7e)

Harikane, Y., Ouchi, M., Oguri, M., et al. 2023, *ApJS*, 265, 5, doi: [10.3847/1538-4365/acaaa9](https://doi.org/10.3847/1538-4365/acaaa9)

Heckman, T. M., & Borthakur, S. 2016, *ApJ*, 822, 9, doi: [10.3847/0004-637X/822/1/9](https://doi.org/10.3847/0004-637X/822/1/9)

Helton, J. M., Sun, F., Woodrum, C., et al. 2024a, *ApJ*, 962, 124, doi: [10.3847/1538-4357/ad0da7](https://doi.org/10.3847/1538-4357/ad0da7)

Helton, J. M., Sun, F., Woodrum, C., et al. 2024b, *ApJ*, 974, 41, doi: [10.3847/1538-4357/ad6867](https://doi.org/10.3847/1538-4357/ad6867)

Hutter, A., Cueto, E. R., Dayal, P., et al. 2025, *A&A*, 694, A254, doi: [10.1051/0004-6361/202452460](https://doi.org/10.1051/0004-6361/202452460)

Inayoshi, K., Harikane, Y., Inoue, A. K., Li, W., & Ho, L. C. 2022, *ApJL*, 938, L10, doi: [10.3847/2041-8213/ac9310](https://doi.org/10.3847/2041-8213/ac9310)

Jiang, T., Malhotra, S., Yang, H., & Rhoads, J. E. 2019, *ApJ*, 872, 146, doi: [10.3847/1538-4357/aaeee79](https://doi.org/10.3847/1538-4357/aaeee79)

Johnson, B. D., Leja, J., Conroy, C., & Speagle, J. S. 2021, *ApJS*, 254, 22, doi: [10.3847/1538-4365/abef67](https://doi.org/10.3847/1538-4365/abef67)

Kennicutt, Jr., R. C. 1998, *ARA&A*, 36, 189, doi: [10.1146/annurev.astro.36.1.189](https://doi.org/10.1146/annurev.astro.36.1.189)

Kocevski, D. D., Onoue, M., Inayoshi, K., et al. 2023, *ApJL*, 954, L4, doi: [10.3847/2041-8213/ace5a0](https://doi.org/10.3847/2041-8213/ace5a0)

Leja, J., Carnall, A. C., Johnson, B. D., Conroy, C., & Speagle, J. S. 2019, *ApJ*, 876, 3, doi: [10.3847/1538-4357/ab133c](https://doi.org/10.3847/1538-4357/ab133c)

Li, Q., Conselice, C. J., Sarron, F., et al. 2025, *MNRAS*, 539, 1796, doi: [10.1093/mnras/staf543](https://doi.org/10.1093/mnras/staf543)

Llerena, M., Amorín, R., Pentericci, L., et al. 2023, *A&A*, 676, A53, doi: [10.1051/0004-6361/202346232](https://doi.org/10.1051/0004-6361/202346232)

Madau, P. 1995, *ApJ*, 441, 18, doi: [10.1086/175332](https://doi.org/10.1086/175332)

Madau, P., & Dickinson, M. 2014, *ARA&A*, 52, 415, doi: [10.1146/annurev-astro-081811-125615](https://doi.org/10.1146/annurev-astro-081811-125615)

Malkan, M. A., Mehta, V., Acharyya, A., et al. 2025, arXiv e-prints, arXiv:2509.00596, doi: [10.48550/arXiv.2509.00596](https://doi.org/10.48550/arXiv.2509.00596)

Mason, C. A., Trenti, M., & Treu, T. 2023, MNRAS, 521, 497, doi: [10.1093/mnras/stad035](https://doi.org/10.1093/mnras/stad035)

Meurer, G. R., Heckman, T. M., & Calzetti, D. 1999, ApJ, 521, 64, doi: [10.1086/307523](https://doi.org/10.1086/307523)

Morishita, T. 2021, ApJS, 253, 4, doi: [10.3847/1538-4365/abce67](https://doi.org/10.3847/1538-4365/abce67)

Morishita, T., Stiavelli, M., Trenti, M., et al. 2020, ApJ, 904, 50, doi: [10.3847/1538-4357/abba83](https://doi.org/10.3847/1538-4357/abba83)

Morishita, T., Stiavelli, M., Chary, R.-R., et al. 2024, ApJ, 963, 9, doi: [10.3847/1538-4357/ad1404](https://doi.org/10.3847/1538-4357/ad1404)

Morishita, T., Mason, C. A., Kreilgaard, K. C., et al. 2025a, ApJ, 983, 152, doi: [10.3847/1538-4357/adb8dc](https://doi.org/10.3847/1538-4357/adb8dc)

Morishita, T., Liu, Z., Stiavelli, M., et al. 2025b, ApJ, 982, 153, doi: [10.3847/1538-4357/adb30f](https://doi.org/10.3847/1538-4357/adb30f)

Naidu, R. P., Oesch, P. A., van Dokkum, P., et al. 2022a, ApJL, 940, L14, doi: [10.3847/2041-8213/ac9b22](https://doi.org/10.3847/2041-8213/ac9b22)

Naidu, R. P., Oesch, P. A., Setton, D. J., et al. 2022b, arXiv e-prints, arXiv:2208.02794, doi: [10.48550/arXiv.2208.02794](https://doi.org/10.48550/arXiv.2208.02794)

Naidu, R. P., Oesch, P. A., Brammer, G., et al. 2025, arXiv e-prints, arXiv:2505.11263, doi: [10.48550/arXiv.2505.11263](https://doi.org/10.48550/arXiv.2505.11263)

Napolitano, L., Castellano, M., Pentericci, L., et al. 2025, A&A, 693, A50, doi: [10.1051/0004-6361/202452090](https://doi.org/10.1051/0004-6361/202452090)

Ono, Y., Ouchi, M., Harikane, Y., et al. 2025, arXiv e-prints, arXiv:2502.08885, doi: [10.48550/arXiv.2502.08885](https://doi.org/10.48550/arXiv.2502.08885)

Ono, Y., Harikane, Y., Ouchi, M., et al. 2024, PASJ, 76, 219, doi: [10.1093/pasj/pvae004](https://doi.org/10.1093/pasj/pvae004)

Peng, C. Y., Ho, L. C., Impey, C. D., & Rix, H.-W. 2002, AJ, 124, 266, doi: [10.1086/340952](https://doi.org/10.1086/340952)

Peng, C. Y., Ho, L. C., Impey, C. D., & Rix, H.-W. 2010, AJ, 139, 2097, doi: [10.1088/0004-6256/139/6/2097](https://doi.org/10.1088/0004-6256/139/6/2097)

Rayner, J. T., Toomey, D. W., Onaka, P. M., et al. 2003, PASP, 115, 362, doi: [10.1086/367745](https://doi.org/10.1086/367745)

Reddy, N. A., Topping, M. W., Shapley, A. E., et al. 2022, ApJ, 926, 31, doi: [10.3847/1538-4357/ac3b4c](https://doi.org/10.3847/1538-4357/ac3b4c)

Reddy, N. A., Sanders, R. L., Shapley, A. E., et al. 2023, ApJ, 951, 56, doi: [10.3847/1538-4357/acd0b1](https://doi.org/10.3847/1538-4357/acd0b1)

Roberts-Borsani, G., Morishita, T., Treu, T., Leethochawalit, N., & Trenti, M. 2022, ApJ, 927, 236, doi: [10.3847/1538-4357/ac4803](https://doi.org/10.3847/1538-4357/ac4803)

Roberts-Borsani, G., Treu, T., Shapley, A., et al. 2024, ApJ, 976, 193, doi: [10.3847/1538-4357/ad85d3](https://doi.org/10.3847/1538-4357/ad85d3)

Roberts-Borsani, G., Oesch, P., Ellis, R., et al. 2025a, arXiv e-prints, arXiv:2508.21708, doi: [10.48550/arXiv.2508.21708](https://doi.org/10.48550/arXiv.2508.21708)

Roberts-Borsani, G., Bagley, M., Rojas-Ruiz, S., et al. 2025b, ApJ, 983, 18, doi: [10.3847/1538-4357/adb860](https://doi.org/10.3847/1538-4357/adb860)

Robertson, B., Johnson, B. D., Tacchella, S., et al. 2024, ApJ, 970, 31, doi: [10.3847/1538-4357/ad463d](https://doi.org/10.3847/1538-4357/ad463d)

Robertson, B. E., Tacchella, S., Johnson, B. D., et al. 2023, Nature Astronomy, 7, 611, doi: [10.1038/s41550-023-01921-1](https://doi.org/10.1038/s41550-023-01921-1)

Rojas-Ruiz, S., Finkelstein, S. L., Bagley, M. B., et al. 2020, ApJ, 891, 146, doi: [10.3847/1538-4357/ab7659](https://doi.org/10.3847/1538-4357/ab7659)

Rojas-Ruiz, S., Bagley, M., Roberts-Borsani, G., et al. 2025, ApJ, 985, 80, doi: [10.3847/1538-4357/adc67d](https://doi.org/10.3847/1538-4357/adc67d)

Salpeter, E. E. 1955, ApJ, 121, 161, doi: [10.1086/145971](https://doi.org/10.1086/145971)

Schlafly, E. F., & Finkbeiner, D. P. 2011, ApJ, 737, 103, doi: [10.1088/0004-637X/737/2/103](https://doi.org/10.1088/0004-637X/737/2/103)

Schlegel, D. J., Finkbeiner, D. P., & Davis, M. 1998, ApJ, 500, 525, doi: [10.1086/305772](https://doi.org/10.1086/305772)

Shen, X., Vogelsberger, M., Boylan-Kolchin, M., Tacchella, S., & Kannan, R. 2023, MNRAS, 525, 3254, doi: [10.1093/mnras/stad2508](https://doi.org/10.1093/mnras/stad2508)

Shibuya, T., Ouchi, M., & Harikane, Y. 2015, ApJS, 219, 15, doi: [10.1088/0067-0049/219/2/15](https://doi.org/10.1088/0067-0049/219/2/15)

Sun, F., Fudamoto, Y., Lin, X., et al. 2025, arXiv e-prints, arXiv:2503.15587, doi: [10.48550/arXiv.2503.15587](https://doi.org/10.48550/arXiv.2503.15587)

Tacchella, S., Finkelstein, S. L., Bagley, M., et al. 2022, ApJ, 927, 170, doi: [10.3847/1538-4357/ac4cad](https://doi.org/10.3847/1538-4357/ac4cad)

Tang, M., Stark, D. P., Chen, Z., et al. 2023, MNRAS, 526, 1657, doi: [10.1093/mnras/stad2763](https://doi.org/10.1093/mnras/stad2763)

Topping, M. W., Stark, D. P., Endsley, R., et al. 2024, MNRAS, 529, 4087, doi: [10.1093/mnras/stae800](https://doi.org/10.1093/mnras/stae800)

Trenti, M., Bradley, L. D., Stiavelli, M., et al. 2011, ApJL, 727, L39, doi: [10.1088/2041-8205/727/2/L39](https://doi.org/10.1088/2041-8205/727/2/L39)

Trenti, M., Bradley, L. D., Stiavelli, M., et al. 2012, ApJ, 746, 55, doi: [10.1088/0004-637X/746/1/55](https://doi.org/10.1088/0004-637X/746/1/55)

van Dokkum, P. G. 2001, PASP, 113, 1420, doi: [10.1086/323894](https://doi.org/10.1086/323894)

Weibel, A., Oesch, P. A., Williams, C. C., et al. 2025, arXiv e-prints, arXiv:2507.06292, doi: [10.48550/arXiv.2507.06292](https://doi.org/10.48550/arXiv.2507.06292)

Williams, C. C., Oesch, P. A., Weibel, A., et al. 2025, ApJ, 979, 140, doi: [10.3847/1538-4357/ad97bc](https://doi.org/10.3847/1538-4357/ad97bc)

Witten, C., Oesch, P. A., McClymont, W., et al. 2025, arXiv e-prints, arXiv:2507.06284, doi: [10.48550/arXiv.2507.06284](https://doi.org/10.48550/arXiv.2507.06284)

Yanagisawa, H., Ouchi, M., Nakajima, K., et al. 2024, arXiv e-prints, arXiv:2411.19893, doi: [10.48550/arXiv.2411.19893](https://doi.org/10.48550/arXiv.2411.19893)

Ziparo, F., Ferrara, A., Sommovigo, L., & Kohandel, M. 2023, MNRAS, 520, 2445, doi: [10.1093/mnras/stad125](https://doi.org/10.1093/mnras/stad125)